Adaptive mapping for high order WENO methods

U S Vevek, Zang B. and New T. H.*

School of Mechanical and Aerospace Engineering, Nanyang Technological University

50 Nanyang Avenue, Singapore 639798

Abstract

In this paper, a novel mapping approach through the use of adaptive mapping functions is introduced for high order weighted essentially non-oscillatory (WENO) methods. The new class of adaptive mapping functions are designed to adjust themselves to the solution based on a simple parameter calculated using the smoothness indicators that are readily available during computation. It is shown that this adaptive nature allows the resultant mapped WENO scheme to maintain sub-stencil weights close to the optimal weights in smooth regions without amplifying the weights of non-smooth stencils containing discontinuities. Therefore, adaptive mapping achieves enhanced accuracy in smooth regions and is more resistant against spurious oscillations near discontinuities. Taylor series analysis of the seventh order finite volume WENO scheme has been performed to demonstrate the loss of accuracy of the original WENO method near critical points. The convergence rates of the seventh order finite volume WENO scheme with adaptive mapping has been shown through a simple numerical example. Excellent results have been obtained for one-dimensional linear advection cases especially over long output times. Improved results have also been obtained for one- and two-dimensional Euler equation test cases.

*Corresponding author: dthnew@ntu.edu.sg

1 Introduction

Hyperbolic conservation laws allow discontinuities to exist as part of the solution. In the case of non-linear hyperbolic laws, discontinuities may develop in finite time and persist even when the initial conditions are smooth [1]. It is well known that any fixed-stencil linear scheme will produce spurious oscillations when applied across a discontinuity. The simplest non-linear scheme is the first-order upwind scheme. While it prevents spurious oscillations, it is prohibitively diffusive because it is only first-order accurate. To improve the accuracy, Harten [2] introduced second-order total variation diminishing (TVD) schemes which were designed to drop to the first-order upwind scheme near discontinuities through the use of limiters. However, TVD schemes reverted to being first-order accurate near *smooth* extrema as well. To remedy the situation, Harten, et al. [3] introduced the essentially non-oscillatory (ENO) schemes which, unlike the TVD schemes, did not 'clip' the smooth extrema and maintained a uniformly high order of accuracy. In essence, an r^{th} order ENO scheme chooses the smoothest stencil to perform a polynomial reconstruction from r possible candidate stencils. The ENO concept was extended by Liu, et al. [4] to develop a class of *weighted* ENO (WENO) schemes which uses a convex combination of all the candidate stencils weighted based on the smoothness of the solution within each stencil. This class of WENO schemes could achieve $\left(r+1\right)^{th}$ order of accuracy in smooth regions. Later, Jiang and Shu [5] proposed a different smoothness indicator and Balsara and Shu [6] improved on it further by showing that a $\left(2r-1\right)^{th}$ order WENO scheme could be constructed from r ENO stencils. This class of WENO schemes is referred to as WENO-JS. In order to achieve the optimal $\left(2r-1\right)^{th}$ order accuracy in smooth regions, the WENO-JS stencil weights ω should approach the optimal stencil weights d at a rate of $\omega = d + O\left(\Delta x^{r-1}\right)$. The proposed smoothness indicators were designed to achieve this rate of convergence.

Henrick, et al. [7] identified a crucial problem with the fifth order $\left(r=3\right)$ WENO-JS scheme: it did not exhibit fifth order convergence near smooth critical points. In the neighbourhood of critical points,

the stencil weights only exhibited $\omega = d + O(\Delta x)$ instead of the required $\omega = d + O(\Delta x^2)$. So, they proposed a mapping function to modify the WENO-JS stencil weights to recover the optimal order of accuracy. This was the first ever mapped WENO method; it is referred to as WENO-M (Note: some works refer to this method as WENO-HAP). Essentially, the mapping process tends to bring the WENO-JS stencil weights ω closer to the optimal weights *d* wherever the solution is deemed to be sufficiently smooth.

Feng, et al. [8] proposed a new class of piecewise *p*olynomial *m*apping functions. This method is referred to the method as WENO-PM*k* where *k* is an integer greater than 1. The key difference between these polynomial mapping functions and the mapping function introduced in Ref. [7] is that the first derivatives of the polynomial functions tend to 0 when ω is close 0. They argued that this property was essential to prevent any amplification of the near-zero weights lest they generate spurious oscillations in the solution. It was shown that WENO-PM6 performed better for both smooth and discontinuous problems compared to WENO-M. The one drawback of this class of mapping functions is that its piecewise nature requires logic operations to be performed during the mapping process. This makes it harder to vectorize the operations and increases the computational cost.

In a later study, Feng, et al. [9] showed that the mapping function proposed in Ref. [7], in fact, belongs to a more general class of mapping functions. This *i*mproved *m*apping method is referred to as WENO-IM(*k*, *A*) where $k \geq 2$ is an even integer and *A* a positive real number. They demonstrated that with a slightly different choice of the parameters for *k* and *A*, better results could be obtained for fifth order. In particular, it was reported that WENO-IM(2,0.1) performed vastly superior to WENO-M for fifth order. Unlike the mapping function of WENO-PM6, the first derivatives of these functions do not vanish at $\omega = 0$. In fact, for WENO-IM(2,0.1), the first derivative of the mapping function at $\omega = 0$ is much larger than that of WENO-M resulting in greater amplification of near-zero weights. It was concluded that the excessive amplification of non-smooth stencils brought about by WENO-IM(2,0.1) made it unsuitable for WENO schemes higher than fifth order. Nevertheless, these

mapping functions could be more efficiently implemented compared to those of WENO-PM since they are not piecewise.

Recently, Wang, et al. [10] proposed yet another class of *r*ational *m*apping functions which combines the favourable features of WENO-PM and WENO-IM. These functions are non-piecewise, and, at the same time, their first derivatives vanish at $\omega = 0$. This method is referred to as WENO-RM(*mnk*) where *m*, *n* and *k* are integer parameters. It was reported that the results obtained with WENO-RM(260) scheme for seventh and ninth order WENO schemes were excellent and free from non-physical oscillations.

The authors in a recent work have reported on an even more general class of smooth rational mapping functions which encompasses the mapping functions of WENO-IM [11]. This method was called WENO-RM(*k*,*m*,*s*). It was shown that for $m \geq 1$, the first derivatives of these mapping functions tend to unity at $\omega = 0$, i.e. these functions are able to preserve the near-zero weights rather than actively suppressing them like WENO-PM*k* or WENO-RM(*mnk*). Improved results were obtained for seventh order WENO using WENO-RM(4,4,20).

Borges, et al. [12] chose to approach the loss of accuracy of WENO-JS near critical points in a different manner. They suggested an alternative procedure to compute the non-linear WENO weights replacing part of the original WENO-JS procedure. This method is known as WENO-Z. The most salient aspect of the WENO-Z approach is that it depends on the local smoothness of the solution by making use of the information available in the WENO-JS smoothness indicators. On the contrary, the traditional mapping approaches mentioned thus far are *insensitive* to the local behaviour of the solution even though the information is available. Therefore, the main focus of this study is to improve the current mapping approach by modifying the mapping functions of WENO-RM(*k*,*m*,*s*) so that the mapping process directly depends on the local smoothness of the solution. This is achieved by using the ratio of the minimum and maximum values of the WENO-JS smoothness indicators to adapt the mapping function more specifically to the solution behaviour.

The paper is organized as follows: the WENO-JS scheme and the mapped WENO approach are introduced in Section 2. The rationale of adaptive mapping functions is discussed in Section 3 and suitable parameters are determined for optimal design of the mapping functions. In Section 4, the performance of the adaptive method is compared with other popular seventh order methods for linear advection and Euler equations cases. Finally, the conclusions are given in Section 5.

2 Preliminaries

2.1 Finite volume methodology

Consider the one dimensional scalar conservation law given in Eq. (1) which is to be solved on the domain $x \in [a,b]$ for $t \geq 0$ given the initial condition $u(x,0) = u_0(x)$.

$$\partial_t u + \partial_x f(u) = 0 \tag{1}$$

In the finite volume (FV) methodology, the domain is discretized into non-overlapping cells. For simplicity, assume that the domain is discretized into N uniform cells of width $\Delta x = (b-a)/N$. The cell centres are denoted by $x_i = a + (i - 1/2)\Delta x$ and the cell boundaries are denoted using half-indices $x_{i\pm 1/2} = x_i \pm \Delta x/2$. The i^{th} cell average $\overline{u_i}$ is defined as follows.

$$\overline{u_i} \equiv \frac{1}{\Delta x} \int_{x_{i-1/2}}^{x_{i+1/2}} u(x)\, dx \tag{2}$$

Integrating Eq. (1) over the i^{th} cell and using definition Eq. (2), an ordinary differential equation (ODE) for $\overline{u_i}$ is obtained (see Eq. (3)). Note that the physical flux function $f(u)$ has been replaced with a numerical flux function $\hat{f}(u^L, u^R)$ where u^L and u^R refer to the left-sided and right-sided limits of the function u. Due to the possible presence of discontinuities, u^L and u^R need not be

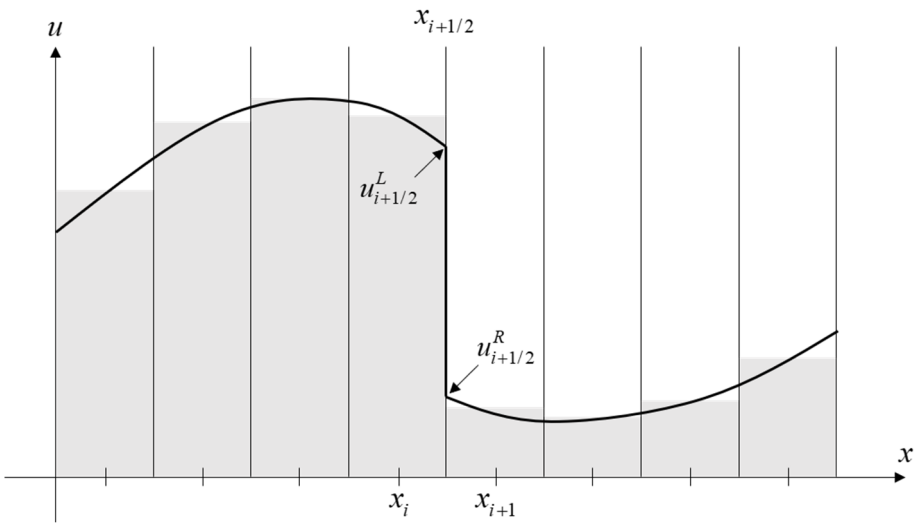

Figure 1: Left- and right-sided approximations of u at cell boundary $x_{i+1/2}$. A discontinuity in u is located at $x_{i+1/2}$. Exact profile is shown by thick black line while cell averages are shown in grey.

equal (see Figure 1). For hyperbolic problems, $\widehat{f}$ needs to be a properly upwinded flux that is consistent with the physical flux, i.e. $\widehat{f}(u,u) = f(u)$.

$$\frac{d\overline{u_i}}{dt} = -\frac{1}{\Delta x}\left[\widehat{f}\left(u^L_{i+1/2}, u^R_{i+1/2}\right) - \widehat{f}\left(u^L_{i-1/2}, u^R_{i-1/2}\right)\right] \tag{3}$$

Once the numerical fluxes are computed, the above ODE can be marched in time using suitable time discretization scheme. In this paper, the third order TVD Runge-Kutta scheme [13] was used for time marching (see Eq. (4)).

$$\begin{aligned} \text{ODE: } & \frac{dq}{dt} = \mathcal{L}(q) \\ & q^{(1)} = q^n + \Delta t \mathcal{L}\left(q^n\right) \\ & q^{(2)} = \frac{3}{4}q^n + \frac{1}{4}\left[q^{(1)} + \Delta t \mathcal{L}\left(q^{(1)}\right)\right] \\ & q^{n+1} = \frac{1}{3}q^n + \frac{2}{3}\left[q^{(2)} + \Delta t \mathcal{L}\left(q^{(2)}\right)\right] \end{aligned} \tag{4}$$

The point values $u^{L/R}_{i\pm1/2}$ required for the computation of numerical fluxes have to be approximated from the neighbouring cell averages and the cells involved in a particular reconstruction will be collectively referred to as a *stencil*. Clearly, the accuracy of the FV method depends directly on the accuracy of the numerical approximations based on these stencils.

2.2 Seventh order upstream central scheme

Consider the approximation of $u_{i+1/2}^{L}$ and assume that $u(x)$ can be approximated by the sixth order polynomial $q(x)$ given in Eq. (5).

$$u(x) \approx q(x) = \sum_{n=0}^{6} a_n x^n \tag{5}$$

The seven unknown coefficients a_n in the polynomial could be obtained by having the polynomial satisfy the cell averages of seven neighbouring cells as shown in Eq. (6). In other words, the solution $u(x)$ is reconstructed using the polynomial $q(x)$.

$$\frac{1}{\Delta x}\int_{x_k-\Delta x/2}^{x_k+\Delta x/2} q(x)\,dx = \overline{u_k} \tag{6}$$

The stencil for the seventh order upstream central scheme for the approximation of $u_{i+1/2}^{L}$ consists of the seven cells $k \in [i-3, \cdots i+3]$. Note that there is one more cell to the left of $x_{i+1/2}$ than to the right in order to provide the necessary left-sided (upstream) biasing. Applying Eq. (6) over the stencil yields a system of linear equations which can be solved to obtain the coefficients a_n. Finally, a_n can be substituted back into Eq. (5) and $q(x)$ can be evaluated at $x_{i+1/2}$ to obtain $u_{i+1/2}^{L,C7} = q(x = x_{i+1/2})$. $u_{i+1/2}^{L,C7}$, which denotes the approximation of $u_{i+1/2}^{L}$ using the seventh order upstream central scheme, is given in Eq. (7). It must be noted that this procedure is considerably simplified if the polynomial is expressed in terms of the non-dimensional parameter $X = (x - x_{i+1/2})/\Delta x$ instead of x. The substitution step would no longer be necessary since $u_{i+1/2}^{L,C7} = q(X = 0) = a_0$.

$$\begin{aligned} u_{i+1/2}^{L,C7} &= \frac{1}{420}\left(-3\overline{u_{i-3}} + 25\overline{u_{i-2}} - 101\overline{u_{i-1}} + 319\overline{u_i} + 214\overline{u_{i+1}} - 38\overline{u_{i+2}} + 4\overline{u_{i+3}}\right) \\ &= u_{i+1/2}^{L} + O\left(\Delta x^7\right) \end{aligned} \tag{7}$$

The upstream central scheme can only be applied in smooth regions of the solution. In the presence of discontinuities and sharp gradients, this scheme results in spurious oscillations in the solution.

2.3 Seventh order WENO-JS scheme

In order to prevent spurious oscillations near discontinuities, WENO schemes use the idea of sub-stencils. In the seventh order WENO scheme, the seven-cell upstream central stencil is divided into four overlapping sub-stencils each consisting of four cells as shown in Figure 2. The solution $u(x)$ is reconstructed using cubic polynomials $p_j(x)$ over each sub-stencil to obtain four fourth order accurate approximations $\left(\hat{u}^L_{i+1/2}\right)_j = p_j\left(x_{i+1/2}\right)$ as shown in Eq. (9).

$$u(x) \approx p_j(x) = \sum_{n=0}^{3} b_{jn} x^n \quad j = [0,1,2,3] \tag{8}$$

$$\begin{aligned}
\left(\hat{u}^L_{i+1/2}\right)_0 &= \frac{1}{12}\left(-3\overline{u_{i-3}} + 13\overline{u_{i-2}} - 23\overline{u_{i-1}} + 25\overline{u_i}\right) \\
&= u^L_{i+1/2} - \frac{1}{5}\frac{\partial^4 u}{\partial x^4}\bigg|_{x_{i+1/2}} \Delta x^4 + \frac{1}{3}\frac{\partial^5 u}{\partial x^5}\bigg|_{x_{i+1/2}} \Delta x^5 - \frac{13}{42}\frac{\partial^6 u}{\partial x^6}\bigg|_{x_{i+1/2}} \Delta x^6 + O\left(\Delta x^7\right) \\
\left(\hat{u}^L_{i+1/2}\right)_1 &= \frac{1}{12}\left(\overline{u_{i-2}} - 5\overline{u_{i-1}} + 13\overline{u_i} + 3\overline{u_{i+1}}\right) \\
&= u^L_{i+1/2} + \frac{1}{20}\frac{\partial^4 u}{\partial x^4}\bigg|_{x_{i+1/2}} \Delta x^4 - \frac{1}{24}\frac{\partial^5 u}{\partial x^5}\bigg|_{x_{i+1/2}} \Delta x^5 + \frac{1}{42}\frac{\partial^6 u}{\partial x^6}\bigg|_{x_{i+1/2}} \Delta x^6 + O\left(\Delta x^7\right) \\
\left(\hat{u}^L_{i+1/2}\right)_2 &= \frac{1}{12}\left(-\overline{u_{i-1}} + 7\overline{u_i} + 7\overline{u_{i+1}} - \overline{u_{i+2}}\right) \\
&= u^L_{i+1/2} - \frac{1}{30}\frac{\partial^4 u}{\partial x^4}\bigg|_{x_{i+1/2}} \Delta x^4 - \frac{1}{252}\frac{\partial^6 u}{\partial x^6}\bigg|_{x_{i+1/2}} \Delta x^6 + O\left(\Delta x^7\right) \\
\left(\hat{u}^L_{i+1/2}\right)_3 &= \frac{1}{12}\left(3\overline{u_i} + 13\overline{u_{i+1}} - 5\overline{u_{i+2}} + \overline{u_{i+3}}\right) \\
&= u^L_{i+1/2} + \frac{1}{20}\frac{\partial^4 u}{\partial x^4}\bigg|_{x_{i+1/2}} \Delta x^4 + \frac{1}{24}\frac{\partial^5 u}{\partial x^5}\bigg|_{x_{i+1/2}} \Delta x^5 + \frac{1}{42}\frac{\partial^6 u}{\partial x^6}\bigg|_{x_{i+1/2}} \Delta x^6 + O\left(\Delta x^7\right)
\end{aligned} \tag{9}$$

The seventh order WENO approximation $u^{L,W7}_{i+1/2}$ is obtained by taking a convex combination of $\left(\hat{u}^L_{i+1/2}\right)_j$ as shown in Eq. (10). ω_j denotes the WENO-JS weight assigned to the j^{th} sub-stencil. These weights should reflect the relative smoothness of the solution reconstructed within that sub-stencil. If a sub-stencil contains a discontinuity, it should be allocated a very small weight so as to effectively remove its contribution. On the other hand, if the solution is smooth in all four sub-

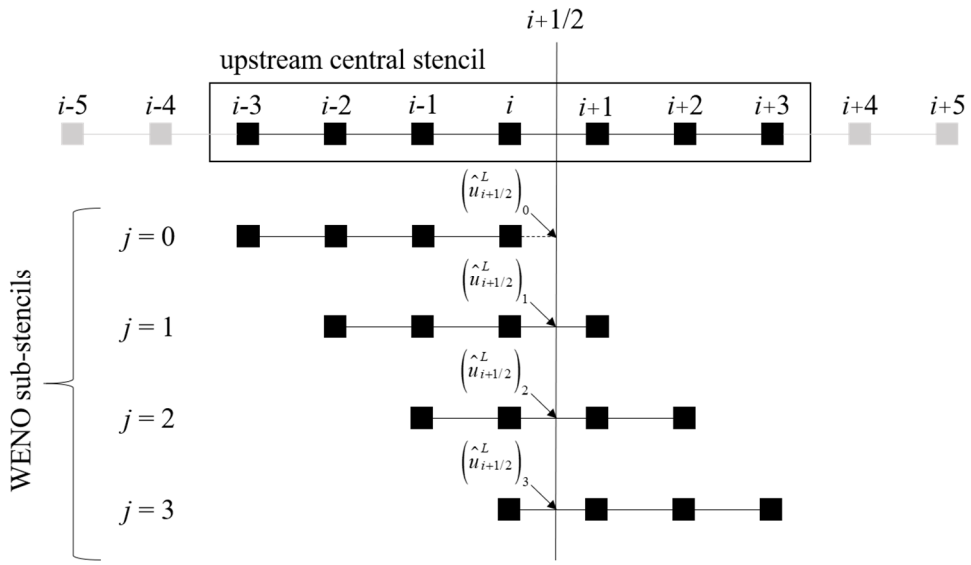

Figure 2: Schematic of seventh order WENO stencils.

stencils, ω_j should be such that $u_{i+1/2}^{L,W7} = u_{i+1/2}^{L,C7} + O\left(\Delta x^7\right)$, i.e. the WENO approximation should recover the optimal seventh order accuracy.

$$u_{i+1/2}^{L,W7} = \sum_{j=0}^{3} \omega_j \left(\hat{u}_{i+1/2}^{L}\right)_j \tag{10}$$

Let d_j denote the optimal weight to allocate to the j^{th} sub-stencil such that $u_{i+1/2}^{L,W7} = u_{i+1/2}^{L,C7}$ exactly. Substituting $\omega_j = d_j$ into Eq. (10) and using the Taylor series expansions of $\left(\hat{u}_{i+1/2}^{L}\right)_j$ from Eq. (9), a linear system of equations can be formed such that the fourth, fifth and sixth order truncation errors are eliminated. The condition that d_j must sum to unity is used to complete the system so that it can be solved for d_j as shown in Eq. (11).

$$\begin{bmatrix} 1 & 1 & 1 & 1 \\ -1/5 & 1/20 & -1/30 & 1/20 \\ 1/3 & -1/24 & 0 & 1/24 \\ -13/42 & 1/42 & -1/252 & 1/42 \end{bmatrix} \begin{Bmatrix} d_0 \\ d_1 \\ d_2 \\ d_3 \end{Bmatrix} = \begin{Bmatrix} 1 \\ 0 \\ 0 \\ 0 \end{Bmatrix} \rightarrow \begin{Bmatrix} d_0 \\ d_1 \\ d_2 \\ d_3 \end{Bmatrix} = \frac{1}{35} \begin{Bmatrix} 1 \\ 12 \\ 18 \\ 4 \end{Bmatrix} \tag{11}$$

As mentioned earlier, ω_j must approach d_j in smooth regions of the solution such that $u_{i+1/2}^{L,W7} = u_{i+1/2}^{L,C7} + O\left(\Delta x^7\right)$. This expression can be expanded as shown in Eq. (12). Subtracting $u_{i+1/2}^{L}$ on

both sides and using the fact that both ω_j and d_j sum to unity, it can be shown that $\omega_j = d_j + O\left(\Delta x^3\right)$ in smooth regions for seventh order convergence.

$$
\begin{aligned}
&u_{i+1/2}^{L,W7} = u_{i+1/2}^{L,C7} + O\left(\Delta x^7\right) \\
&\sum_{j=0}^{3} \omega_j \left(\hat{u}_{i+1/2}^{L}\right)_j = \sum_{j=0}^{3} d_j \left(\hat{u}_{i+1/2}^{L}\right)_j + O\left(\Delta x^7\right) \\
&\sum_{j=0}^{3} \omega_j \left(\hat{u}_{i+1/2}^{L}\right)_j - u_{i+1/2}^{L} \sum_{j=0}^{3} \omega_j = \sum_{j=0}^{3} d_j \left(\hat{u}_{i+1/2}^{L}\right)_j - u_{i+1/2}^{L} \sum_{j=0}^{3} d_j + O\left(\Delta x^7\right) \\
&\sum_{j=0}^{7} \left(\omega_j - d_j\right) \underbrace{\left[\left(\hat{u}_{i+1/2}^{L}\right)_j - u_{i+1/2}^{L}\right]}_{O\left(\Delta x^4\right) \text{ [Eq. (8)]}} = O\left(\Delta x^7\right) \Rightarrow \omega_j = d_j + O\left(\Delta x^3\right)
\end{aligned}
\tag{12}
$$

With the appropriate relationship between ω_j and determined, consider a sub-stencil smoothness indicator IS_j of the form $IS_j = D\left[K + O\left(\Delta x^3\right)\right]$ where *D* and *K* are non-zero constants independent of j. These smoothness indicators can be used to define WENO-JS weights as shown in Eq. (13). ϵ is a small number used to prevent division by 0. Notice that ω_j and d_j satisfy the required relationship that was derived in Eq. (12).

$$
\alpha_j = \frac{d_j}{\left(IS_j + \epsilon\right)^r} = \frac{d_j}{\left(DK\right)^r}\left[1 + O\left(\Delta x^3\right)\right] \qquad \omega_j = \frac{\alpha_j}{\sum_{j=0}^{3} \alpha_j} = d_j + O\left(\Delta x^3\right) \tag{13}
$$

Following Ref. [5], IS_j is defined as follows. Interested readers are referred to Appendix A for derivation of IS_j in their explicit forms in terms of the cell averages.

$$
IS_j = \sum_{k=1}^{3} \int_{x_{i-1/2}}^{x_{i+1/2}} \Delta x^{2k-1} \left[\frac{d^k p_j(x)}{dx^k}\right]^2 dx \tag{14}
$$

Expanding the smoothness indicators using Taylor series about $x = x_i$ yields the expressions shown in Eq. (15). Let n_{cp} denote the number of derivatives which vanish at $x = x_i$, i.e. $\partial^k u / \partial x^k = 0$ for all $k \in \left[1, n_{cp}\right]$. $n_{cp} = 0$ means that $\partial u / \partial x \neq 0$ at the concerned location. Let r_c refer to the order of

convergence of the approximation. As shown in Table 1, the smoothness indicators are of the correct form $IS_j = D\left[K + O\left(\Delta x^3\right)\right]$ only when $n_{cp} = 0$, i.e. away from critical points. As each subsequent derivative vanishes, the order of convergence is reduced by one order. Therefore, WENO-JS suffers from a loss of accuracy near critical points.

$$
\begin{aligned}
IS_0 &= \left(\frac{\partial u}{\partial x}\right)^2 \Delta x^2 + \left[\frac{13}{12}\left(\frac{\partial^2 u}{\partial x^2}\right)^2 + \frac{1}{12}\frac{\partial u}{\partial x}\frac{\partial^3 u}{\partial x^3}\right]\Delta x^4 - \frac{1}{2}\frac{\partial u}{\partial x}\frac{\partial^4 u}{\partial x^4}\Delta x^5 \\
&\quad + \left[\frac{1043}{960}\left(\frac{\partial^3 u}{\partial x^3}\right)^2 - \frac{91}{48}\frac{\partial^2 u}{\partial x^2}\frac{\partial^4 u}{\partial x^4} + \frac{577}{960}\frac{\partial u}{\partial x}\frac{\partial^5 u}{\partial x^5}\right]\Delta x^6 + O\left(\Delta x^7\right) \\
IS_1 &= \left(\frac{\partial u}{\partial x}\right)^2 \Delta x^2 + \left[\frac{13}{12}\left(\frac{\partial^2 u}{\partial x^2}\right)^2 + \frac{1}{12}\frac{\partial u}{\partial x}\frac{\partial^3 u}{\partial x^3}\right]\Delta x^4 + \frac{1}{6}\frac{\partial u}{\partial x}\frac{\partial^4 u}{\partial x^4}\Delta x^5 \\
&\quad + \left[\frac{1043}{960}\left(\frac{\partial^3 u}{\partial x^3}\right)^2 + \frac{13}{48}\frac{\partial^2 u}{\partial x^2}\frac{\partial^4 u}{\partial x^4} - \frac{21}{320}\frac{\partial u}{\partial x}\frac{\partial^5 u}{\partial x^5}\right]\Delta x^6 + O\left(\Delta x^7\right) \\
IS_2 &= \left(\frac{\partial u}{\partial x}\right)^2 \Delta x^2 + \left[\frac{13}{12}\left(\frac{\partial^2 u}{\partial x^2}\right)^2 + \frac{1}{12}\frac{\partial u}{\partial x}\frac{\partial^3 u}{\partial x^3}\right]\Delta x^4 - \frac{1}{6}\frac{\partial u}{\partial x}\frac{\partial^4 u}{\partial x^4}\Delta x^5 \\
&\quad + \left[\frac{1043}{960}\left(\frac{\partial^3 u}{\partial x^3}\right)^2 + \frac{13}{48}\frac{\partial^2 u}{\partial x^2}\frac{\partial^4 u}{\partial x^4} - \frac{21}{320}\frac{\partial u}{\partial x}\frac{\partial^5 u}{\partial x^5}\right]\Delta x^6 + O\left(\Delta x^7\right) \\
IS_3 &= \left(\frac{\partial u}{\partial x}\right)^2 \Delta x^2 + \left[\frac{13}{12}\left(\frac{\partial^2 u}{\partial x^2}\right)^2 + \frac{1}{12}\frac{\partial u}{\partial x}\frac{\partial^3 u}{\partial x^3}\right]\Delta x^4 + \frac{1}{2}\frac{\partial u}{\partial x}\frac{\partial^4 u}{\partial x^4}\Delta x^5 \\
&\quad + \left[\frac{1043}{960}\left(\frac{\partial^3 u}{\partial x^3}\right)^2 - \frac{91}{48}\frac{\partial^2 u}{\partial x^2}\frac{\partial^4 u}{\partial x^4} + \frac{577}{960}\frac{\partial u}{\partial x}\frac{\partial^5 u}{\partial x^5}\right]\Delta x^6 + O\left(\Delta x^7\right)
\end{aligned}
\tag{15}
$$

Table 1: Behaviour of smoothness indicators and WENO-JS weights away from and at critical points

	$n_{cp} = 0$	$n_{cp} = 1$	$n_{cp} = 2$
IS_j	$\left(\frac{\partial u}{\partial x}\right)^2 \Delta x^2\left[K + O\left(\Delta x^3\right)\right]$	$\frac{13}{12}\left(\frac{\partial^2 u}{\partial x^2}\right)^2 \Delta x^4\left[K + O\left(\Delta x^2\right)\right]$	$\frac{1043}{960}\left(\frac{\partial^3 u}{\partial x^3}\right)^2 \Delta x^6\left[K + O\left(\Delta x\right)\right]$
ω_j	$d_j + O\left(\Delta x^3\right)$	$d_j + O\left(\Delta x^2\right)$	$d_j + O\left(\Delta x\right)$
r_c	7	6	5

2.4 The mapped WENO approach

The discrepancy in WENO-JS near critical points was first discovered by Henrick, et al. [7] for the fifth order WENO-JS scheme. They proposed a mapped WENO approach, WENO-M, to recover the loss of accuracy that occurs near critical points. It involves two additional steps after the calculation of the WENO-JS weights ω_j. First, a mapping of the WENO-JS weights is performed with the use of a mapping function $g:\omega_j \to \widetilde{\alpha_j}$. Second, the mapped values $\widetilde{\alpha_j}$ are normalized as shown below so that the mapped weights $\widetilde{\omega_j}$ sum to unity. Finally, $u_{i+1/2}^{L,W7}$ is obtained by using Eq. (10) with $\widetilde{\omega_j}$ instead of ω_j. In fact, one can even view WENO-JS itself to be a mapped WENO method with the mapping function $g_{\mathrm{JS}}(\omega)=\omega$, i.e. the identity map.

$$\widetilde{\omega_j}=\frac{\widetilde{\alpha_j}}{\sum_{j=0}^{2}\widetilde{\alpha_j}} \tag{16}$$

The mapping function for WENO-M is given in Eq. (17). The subscript *j* will be dropped from *d* and ω for conciseness.

$$g_{\mathrm{M}}(\omega)=\frac{\omega\left[d+d^2-3d\omega+\omega^2\right]}{d^2+(1-2d)\omega} \tag{17}$$

$g_{\mathrm{M}}(\omega)$ satisfies the following properties:

(a) $g_{\mathrm{M}}(0)=0$, $g_{\mathrm{M}}(d)=d$ and $g_{\mathrm{M}}(1)=1$

(b) monotone increasing with finite slopes for $\omega\in[0,1]$

(c) $g_{\mathrm{M}}'(d)=g_{\mathrm{M}}''(d)=0$, i.e. function flattens in the vicinity of $\omega=d$

It is noteworthy that the identity map satisfies properties (a) and (b) but not (c). Referring to Figure 3, it becomes clear that the flattening of the function near $d=12/35$ causes any non-linear weight ω within a certain range of *d* to be mapped to a value very close to *d* itself. In other words, the mapping

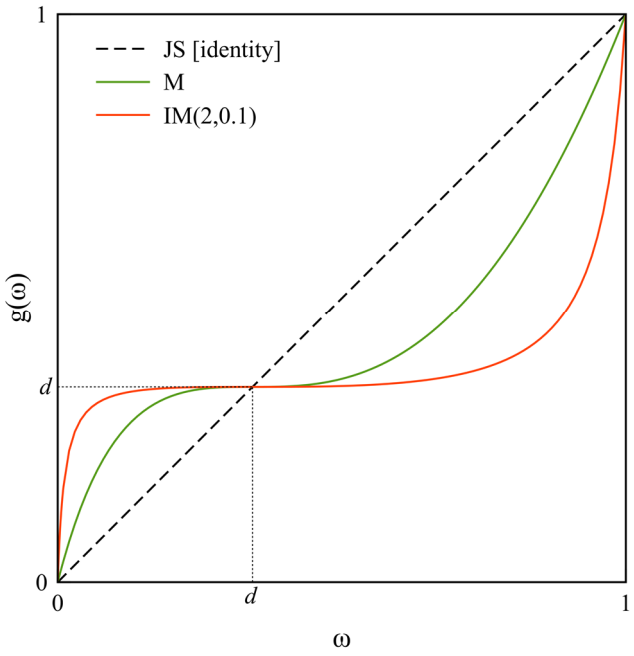

Figure 3: Comparison of mapping functions for d =12/35

process attempts to use the optimal weights over a wider range about $\omega = d$ compared to WENO-JS, bringing the scheme closer to the upstream central scheme. This range will be referred to as the *central range* henceforth.

Since the introduction of WENO-M, several variations have been developed. These variants differ in the choice of mapping functions g. Feng, et al. [9] introduced a broader class of *i*mproved *m*apping functions $g_{\mathrm{IM}}(\omega; k, A)$, shown in Eq. (18), where k is an even integer and A a positive number. $g_{\mathrm{IM}}(\omega; k, A)$ includes $g_{\mathrm{M}}(\omega)$ as a special case when $k = 2$ and $A = 1$. Note that $g_{\mathrm{IM}}(\omega; k, A)$ satisfies an extension of property (c) whereby $g'_{\mathrm{IM}}(d) = \cdots = g^{(k)}_{\mathrm{IM}}(d) = 0$.

$$g_{\mathrm{IM}}(\omega; k, A) = d + \frac{A(\omega - d)^{k+1}}{A(\omega - d)^{k} + \omega(1-\omega)} \tag{18}$$

Feng, et al. [9] found that by taking $k = 2$ and $A = 0.1$, far better results could be obtained for the fifth order WENO method as compared to WENO-M. It is evident from Figure 3 that $g_{\mathrm{IM}}(\omega; 2, 0.1)$ has a much wider central range compared to $g_{\mathrm{M}}(\omega)$. It was postulated that the wider central range is the reason for the superior performance of WENO-IM(2,0.1), especially over long output times.

However, they also reported that WENO-IM(2,0.1) performed poorly for higher order (seventh and above) WENO schemes due to the possible over-amplification of the contributions from non-smooth stencils and recommended the use of WENO-M for higher orders. It can be noticed from Figure 3 that while both $g_{\mathrm{M}}(\omega)$ and $g_{\mathrm{IM}}(\omega; 2, 0.1)$ amplify weights close to 0, the amplification due to $g_{\mathrm{IM}}(\omega; 2, 0.1)$ is greater since $g'_{\mathrm{IM}}(0; 2, 0.1) > g'_{\mathrm{M}}(0)$. This amplification exists even for fifth order WENO. However, it becomes more severe at higher orders due to the smaller numerical values of d (see Eq. (19)). For instance, the smallest optimal weight for the seventh order WENO (1/35) when substituted into Eq. (19) for $k = 2$ and $A = 0.1$ results in an amplification of approximately 351 times while the smallest optimal weight for fifth order WENO (1/10) results in an amplification of approximately 101 times. Excessive amplification of the weights of non-smooth stencils causes spurious oscillations to occur in the solution which may even render the algorithm unstable.

$$g'_{\mathrm{IM}}(0; k, A) = 1 + \frac{1}{Ad^{k-1}} \tag{19}$$

Nevertheless, it is apparent from the success of WENO-IM(2,0.1) for fifth order that widening the central range results in better performance. However, it also increases the risk of the scheme not possessing sufficient numerical viscosity near discontinuities leading to the appearance of spurious oscillations at higher orders. The ideal solution would be to maintain a large central range in smooth regions and a smaller, and yet stable, one near discontinuities. With this idea in mind, a new class of adaptive mapping functions is introduced in the present paper.

3 Design and properties of adaptive mapping functions

3.1 Rationale of adaptive mapping

Consider a general class of *r*ational *m*apping functions $g_{\mathrm{RM}}(\omega; k, m, s)$ shown in Eq. (20) where k is a positive even integer, m a positive integer and s a positive real number. It can be verified easily

that $g_{\mathrm{IM}}(\omega; k, A) = g_{\mathrm{RM}}\left(\omega; k, 1, A^{-1}\right)$. The effects of varying the parameters k, m and s are shown in Figure 4.

$$g_{\mathrm{RM}}(\omega; k, m, s) = d + \frac{(\omega - d)^{k+1}}{(\omega - d)^{k} + s\left[\omega(1-\omega)\right]^{m}} \tag{20}$$

$g_{\mathrm{RM}}(\omega; k, m, s)$ possesses the following properties:

(a) $g_{\mathrm{RM}}(0; k, m, s) = 0$, $g_{\mathrm{RM}}(d; k, m, s) = d$ and $g_{\mathrm{RM}}(1; k, m, s) = 1$

(b) monotone increasing with finite slopes for $\omega \in [0, 1]$ when $k \geq m - 1$ [1]

(c) $g'_{\mathrm{RM}}(d; k, m, s) = \cdots = g^{(k)}_{\mathrm{RM}}(d; k, m, s) = 0$

(d) $g'_{\mathrm{RM}}(0; k, m, s) = g'_{\mathrm{RM}}(1; k, m, s) = 1$ for $m > 1$

While properties (a)-(c) are satisfied by other mapped WENO methods as well, property (d) is unique to $g_{\mathrm{RM}}(\omega; k, m, s)$. For a given k and s, increasing m causes the function to follow the identity map more closely near $\omega = 0$ and $\omega = 1$. It also narrows the central range. On the other hand, for a given m and s, increasing k widens the central range since more derivatives vanish at $\omega = d$. Therefore, increasing k and increasing m have opposite effects on the shape of the mapping function. Using $g_{\mathrm{RM}}(\omega; k, m, s)$ with $m > 1$ might be more suitable for higher order WENO schemes since the function is able to preserve near-zero weights without large amplifications. Indeed, it was found that $g_{\mathrm{RM}}(\omega; 4, 4, 20)$, for instance, outperformed both $g_{\mathrm{M}}(\omega)$ and $g_{\mathrm{IM}}(\omega; 2, 0.1)$ for seventh order WENO. Nevertheless, it was unable to prevent the development of spurious oscillations over long output times in advection problems [11].

The traditional mapped WENO approach discussed thus far uses a fixed mapping function. However, as mentioned earlier, a mapping function should ideally apply the optimal weights wherever possible without causing spurious oscillations to appear near discontinuities. An adaptive mapping function

[1] Refer to Appendix B for proof.

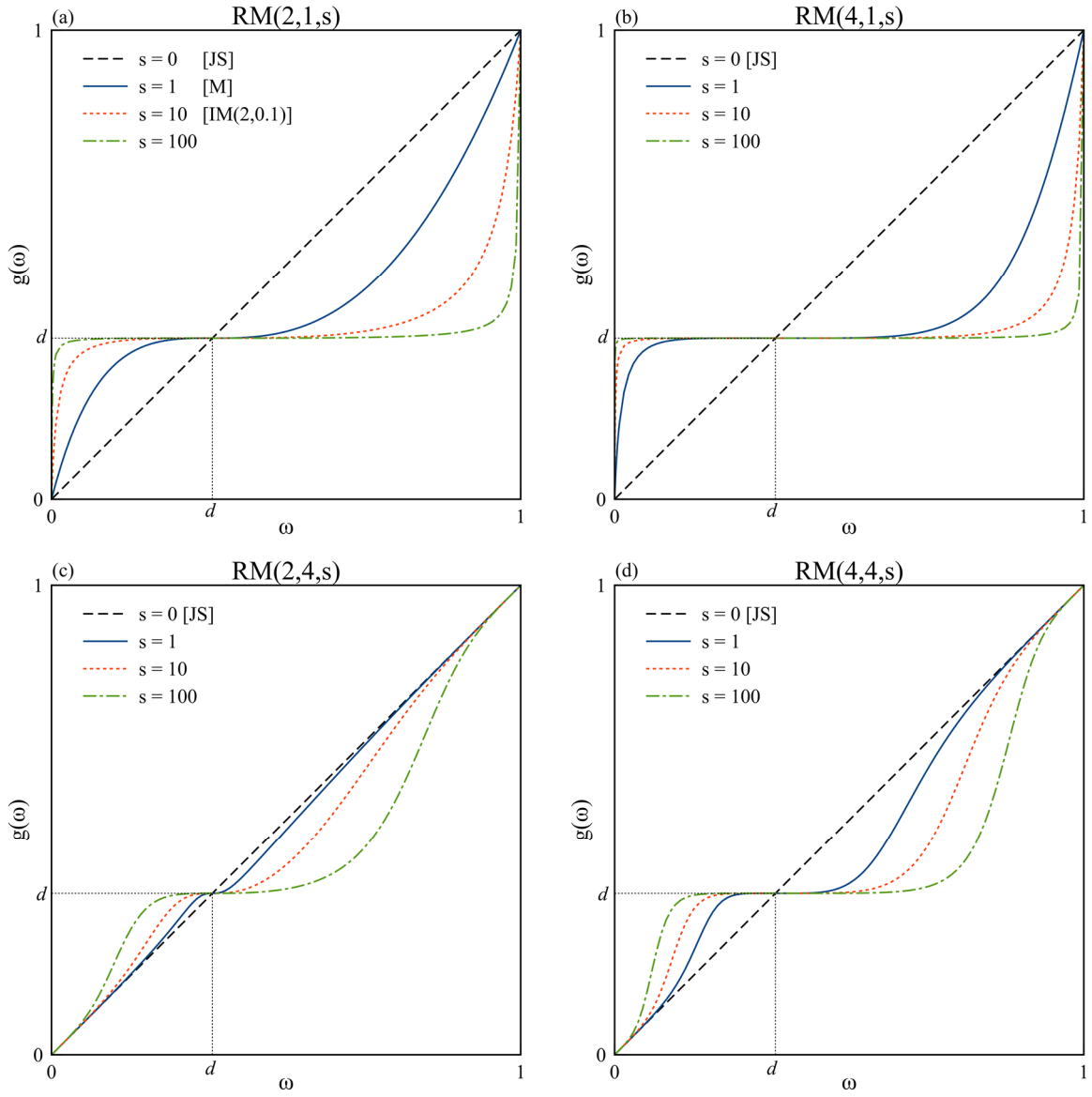

Figure 4: Effect of varying parameters k, m and s on $\mathbf{g}_{\mathrm{RM}}$ for d=12/35

with a variable central range might solve this problem. Referring back to Figure 4, it can be observed that for a given k and m, increasing s widens the central range. As $s \to 0$, $g_{\mathrm{RM}}(\omega; k, m, s)$ approaches the identity map (WENO-JS). This provides an opportunity to *adapt* the mapping function based on the local smoothness of the solution by making the parameter s in Eq. (20) to be proportional to the ratio of the minimum to the maximum values of the smoothness indicators IS_j, i.e.

$$s \propto \lambda \quad \text{where } \lambda = \frac{\min\left(IS_j\right)}{\max\left(IS_j\right) + \epsilon_m} \tag{21}$$

When the solution is smooth, λ is close to 1 resulting in wide central range which allows the mapped weights to be nearly equal to the central weights. On the other hand, when the solution is discontinuous, λ is approximately 0 which causes the central range to narrow preventing excessive amplification of the non-smooth stencils. Adaptive mapping makes use of the information present in the smoothness indicators that is readily available during the interpolation process. Note that a parameter similar to λ has been used in [14, 15] to assess the local behaviour of the solution.

The parameter ϵ_m in Eq. (21) is a small number that is different from ϵ used in Eq. (13). ϵ_m provides a threshold of significance for the smoothness indicators, i.e. if $\max\left(IS_j\right) \ll \epsilon_m$, $\lambda \approx 0$ regardless of the values of the smoothness indicators. If a relatively large value such as $\epsilon_m = 10^{-6}$ is used, it may overpower the subtle differences in the smoothness indicators and cause the scheme to revert to the WENO-JS scheme quickly. On the other hand, using a very small value such as $\epsilon_m = 10^{-40}$ may accentuate numerical noise. Therefore, a mesh-dependent value of $\epsilon_m = \Delta x^7$ has been chosen since it is clear from the Taylor series analysis shown in Eq (15) that the smoothness indicators are dependent on Δx. Indeed, this choice, as demonstrated later in the numerical experiments, performs well for all difference cases at various resolutions.

During initial tests, the adapting parameter *s* was simply taken to be λ scaled by a suitable constant *c*. However, it was discovered later that incorporating the inverse of the optimal weight *d* as shown in Eq. (22) results in a drastic reduction of spurious oscillations near sharp discontinuities for advection problems. The intuition behind this choice and a possible explanation for its superior performance will be discussed in Section 3.3.

$$s = cd^{-1}\lambda \tag{22}$$

This will be referred to as the *a*daptive *i*mproved *m*apping WENO method or WENO-AIM(*k*, *m*, *c*).

3.2 Parametric study

With adaptive parameter *s* defined, a parametric study was performed to determine optimal values for parameters *k*, *m* and *c*. The one dimensional linear advection problem (Eq. (23)) was used in this study. In the FV methodology, the cell average $\overline{u_i}$ is evolved at each time step by summing up the numerical fluxes at the cell interfaces $x_{i\pm1/2}$. For the linear advection case, the numerical flux is simply the left-biased interpolation of *u* at the cell interface, i.e. $\hat{f}\left(u^L, u^R\right) = u^L_{i+1/2}$.

$$\partial_t u + \partial_x u = 0 \tag{23}$$

The advection problem was solved with the following two initial conditions. Case 1 simply consists of two constant states separated by sharp discontinuities at $x = 0, \pm 1$ and Case 2, obtained from [5], consists of four profiles – Gaussian, square wave, triangle wave and half-ellipse.

Case 1

$$u_0(x) = \begin{cases} 1 & -1 \le x < 0 \\ 0 & 0 \le x \le 1 \end{cases} \tag{24}$$

Case 2

$$u_0(x) = \begin{cases} \frac{1}{6}\left[G(x,+\delta) + G(x,-\delta) + 4G(x,0)\right] & -0.8 \le x \le -0.6 \\ 1 & -0.4 \le x \le -0.2 \\ 1 - \left|10(x-0.1)\right| & 0 \le x \le 0.2 \\ \frac{1}{6}\left[F(x,+\delta) + F(x,-\delta) + 4F(x,0)\right] & 0.4 \le x \le 0.6 \\ 0 & \text{otherwise} \end{cases} \tag{25}$$

where $G(x,z) = \exp\left[-\frac{\log 2}{36\delta^2}\left(x + 0.7 - z\right)^2\right]$, $F(x,a) = \sqrt{\max\left[0, 1 - 100\left(x - 0.5 - a\right)^2\right]}$ and $\delta = 0.005$.

Both cases were solved on the domain $x \in [-1, 1]$ with periodic boundaries until *t* = 2000s (1000 cycles). The Courant number was fixed at 0.1. The cases were simulated at two different resolutions of *N* = 200 and 400 cells. At the end of the simulations, the L_1 error norms were computed using Eq. (26) where $\overline{u_{0i}}$ is the exact cell average that was used to initialize the problem.

$$\left\| error \right\|_1 = \frac{1}{N} \sum_{i=0}^{N-1} \left| \overline{u_i} - \overline{u_{0i}} \right| \tag{26}$$

Table 2: L1 norms for linear advection Case 1 for $N = 200$ cells

		c					
k	m	1e3	2e3	5e3	1e4	2e4	5e4
2	2	2.5419e-2	2.5387e-2	2.5349e-2	2.5325e-2	2.5303e-2	2.5276e-2
	3	2.5537e-2	2.5501e-2	2.5459e-2	2.5430e-2	2.5404e-2	2.5374e-2
4	2	2.5385e-2	2.5357e-2	2.5325e-2	2.5303e-2	2.5283e-2	2.5260e-2
	3	2.5496e-2	2.5466e-2	2.5428e-2	2.5404e-2	2.5381e-2	2.5354e-2
	4	2.5593e-2	2.5561e-2	2.5522e-2	2.5494e-2	2.5468e-2	2.5437e-2
	5	2.5673e-2	2.5642e-2	2.5603e-2	2.5575e-2	2.5548e-2	2.5515e-2

Table 3: L1 norms for linear advection Case 2 for $N = 200$ cells

		c					
k	m	1e3	2e3	5e3	1e4	2e4	5e4
2	2	6.0671e-2	5.9952e-2	5.9450e-2	5.7990e-2	5.7455e-2	5.5987e-2
	3	7.1935e-2	6.8370e-2	5.9080e-2	5.8358e-2	5.8458e-2	5.7765e-2
4	2	5.9688e-2	5.9361e-2	5.8651e-2	5.8372e-2	5.7917e-2	5.7470e-2
	3	7.1474e-2	6.0102e-2	5.9200e-2	5.9001e-2	5.8173e-2	5.7043e-2
	4	7.2262e-2	6.9789e-2	5.8311e-2	5.8422e-2	5.7140e-2	5.7600e-2
	5	7.6746e-2	7.3716e-2	7.0914e-2	6.8002e-2	5.9469e-2	6.0682e-2

In order to recover the optimal seventh order accuracy even at $n_{cp} = 2$, k must be greater than or equal to 2, and parameter m is bounded between 2 and $k + 1$ (refer to mapping function properties (b) and (d) in Section 3.1). As a result, two values of $k = 2, 4$ and the corresponding m were studied together with six values of the constant c from 1e3 to 5e4 were studied. Tables 2 to 5 summarize the L_1 error norms of the two cases at the two resolutions.

One of the most prominent trends is that increasing m always seems to be result in a greater error regardless of the values of k and c. Therefore, m was chosen to be 2. Secondly, increasing c always results in a lower error for the Case 1 at both resolutions. While a similar trend is observed for Case 2 at $N = 200$, the errors do not always follow this trend at $N = 400$. It was pointed out earlier that increasing m shrinks the central range of the mapping function while increasing s, which is proportional to c, has the opposite effects of widening it. Therefore, it appears that a large central

Table 4: L1 norms for linear advection Case 1 for $N = 400$ cells

		c					
k	m	1e3	2e3	5e3	1e4	2e4	5e4
2	2	1.4007e-2	1.4012e-2	1.3996e-2	1.3985e-2	1.3975e-2	1.3963e-2
	3	1.4081e-2	1.4065e-2	1.4046e-2	1.4032e-2	1.4020e-2	1.4007e-2
4	2	1.4012e-2	1.4000e-2	1.3985e-2	1.3975e-2	1.3966e-2	1.3955e-2
	3	1.4043e-2	1.4034e-2	1.4031e-2	1.4020e-2	1.4010e-2	1.3998e-2
	4	1.4103e-2	1.4091e-2	1.4462e-2	1.4181e-2	1.4208e-2	1.4211e-2
	5	1.4136e-2	1.4128e-2	1.4110e-2	1.4407e-2	1.4404e-2	1.4323e-2

Table 5: L1 norms for linear advection Case 2 for $N = 400$ cells

		c					
k	m	1e3	2e3	5e3	1e4	2e4	5e4
2	2	2.5115e-2	2.7049e-2	2.6734e-2	2.5739e-2	2.4985e-2	2.5030e-2
	3	2.5554e-2	2.5413e-2	2.5732e-2	2.4931e-2	2.4351e-2	2.5758e-2
4	2	2.4951e-2	2.4920e-2	2.5211e-2	2.5271e-2	2.5432e-2	2.5433e-2
	3	2.5450e-2	2.5439e-2	2.5446e-2	2.5442e-2	2.7822e-2	2.7538e-2
	4	2.5341e-2	2.5424e-2	2.5588e-2	2.5612e-2	2.5706e-2	2.5634e-2
	5	2.6777e-2	2.5580e-2	2.5602e-2	2.5831e-2	2.5805e-2	2.5766e-5

range, and hence a large value of c, is vital for improved accuracy. This reinforces the validity of this family of mapped WENO methods. However, increasing c also increases the risk of spurious oscillations. In fact, in some of the cases, the error norms were observed to drop with increasing c despite the formation of noticeable spurious oscillations. Therefore, in addition to a small error norm, resistance to spurious oscillations and other distortions is important. Amazingly, no spurious oscillations or distortions was observed for Case 1 at both resolutions even at $t = 2000$s except for the cases underlined in Table 4. However, the numerical schemes were susceptible to developing small spurious oscillations for Case 2, particularly near the foot of the Gaussian profile. Eventually, the parameters k and c were chosen to be 4 and 1e4, respectively, for a good balance between accuracy and stability. For the remainder of this section, some important properties of WENO-AIM(4,2,1e4) will be discussed.

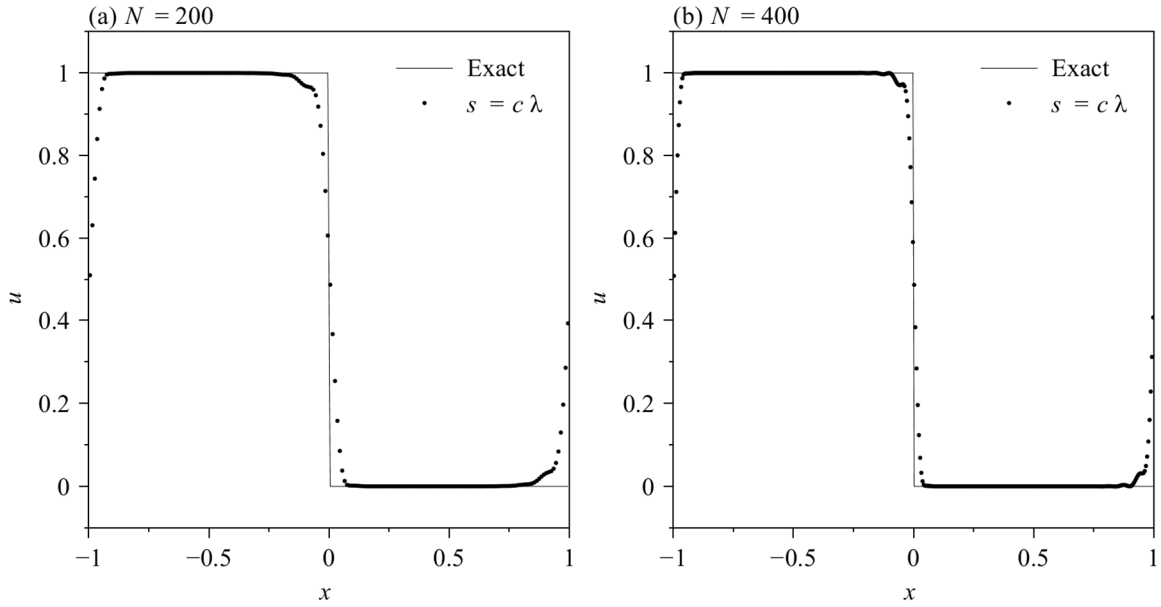

Figure 5: Results for linear advection Case 1 at $t = 1000s$ for (a) $N = 200$ and (b) $N = 400$ cells simulated with WENO-AIM(4,2,1e4) using $s = c\lambda$

3.3 Intuition behind incorporating optimal weight d in parameter s

The effect of introducing the optimal weight in parameter s can be illustrated using the linear advection Case 1. Figure 5 shows the results for case 1 at two different resolutions $N = 200$ and 400 cells at t = 1000s (500 cycles) using $s = c\lambda$. It can be observed that the profile becomes severely distorted to the left (upstream) of the smeared discontinuities at $x = 0$ and $x = 1$ but remains well-behaved to the right (downstream) of the discontinuities. Such asymmetry could possibly stem from the asymmetric assignment of optimal weights. As one approaches a smeared discontinuity from left (i.e. the rightmost sub-stencil being the least smooth), the smoothness indicators increase by a few orders of magnitudes progressively from left to right. For simplicity, the smoothness indicators are assumed to vary as follow.

$$IS_0 = 10^{-14}, \quad IS_2 = 10^{-13}, \quad IS_2 = 10^{-12}, \quad IS_3 = 10^{-10} \tag{27}$$

Note that $\lambda \approx 10^{-4}$ in this case. As one moves away from the smeared discontinuity to the right, the variation of smoothness indicators is reversed, i.e. the leftmost sub-stencil now becomes the least smooth. Ideally, the least smooth sub-stencils in both instances are allocated with approximately

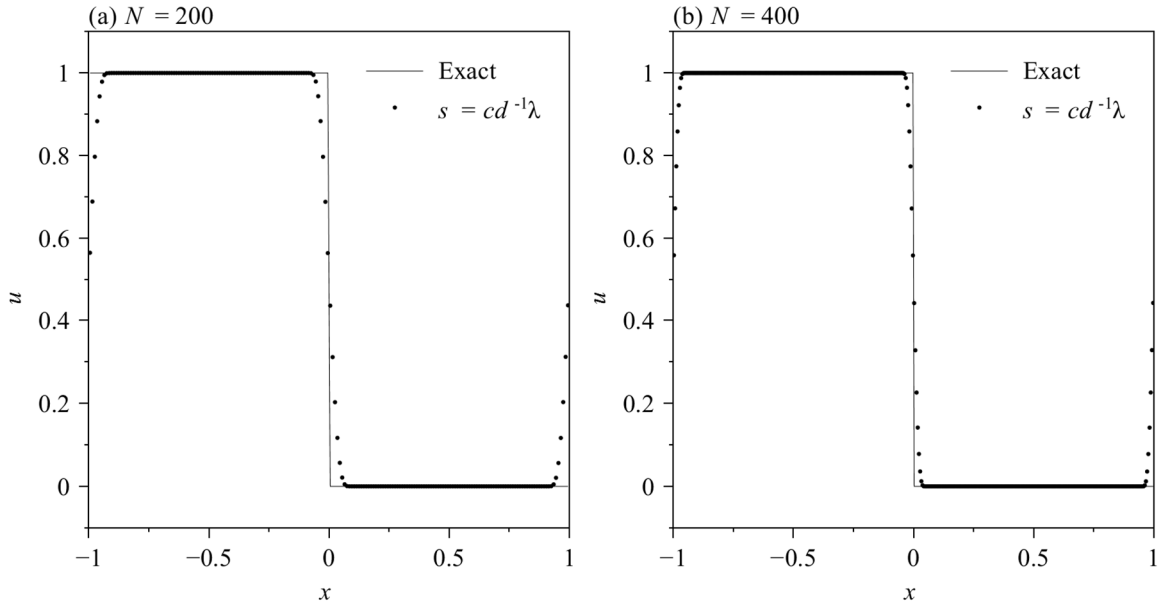

Figure 6: Results for linear advection Case 1 at $t = 1000s$ for (a) $N = 200$ and (b) $N = 400$ cells simulated with WENO-AIM(4,2,1e4) using $s = cd^{-1}\lambda$

similar weights under this simple reflection. However, a quick calculation using $k = 4$, $m = 2$ and $c = 1e4$ with $s = c\lambda$ shows that the weight allocated to the most non-smooth sub-stencil is about 3.81 times larger in the former situation (before reflection) than the latter (after reflection). This disparity is believed to be the cause of the distortions shown in Figure 5. Moreover, the fact that $d_3/d_0 = 4$ not only lends further credibility to this argument, but also points to a plausible remedy.

For small values of ω, the rational mapping function could be approximated as shown in Eq. (28). When ω is extremely small, the first terms in the numerator and denominator are the dominant ones and, consequently, $g_{\mathrm{RM}}(\omega) \approx \omega$ follows the WENO-JS scheme. However, for small values of d, it is possible that both terms are of nearly the same order resulting in the above described disparity.

$$g_{\mathrm{RM}}(\omega; k, m, s = c\lambda) \approx \frac{d^k\omega + sd\omega^m}{d^k + s\omega^m} = \frac{d^k\omega + c\lambda d\omega^m}{d^k + c\lambda\omega^m} \tag{28}$$

One way to overcome this situation is to introduce the inverse of the optimal weight d into parameter s as shown in Eq. (29).

$$g_{\mathrm{RM}}(\omega; k, m, s = cd^{-1}\lambda) \approx \frac{d^k\omega + c\lambda\omega^m}{d^k + c\lambda d^{-1}\omega^m} \tag{29}$$

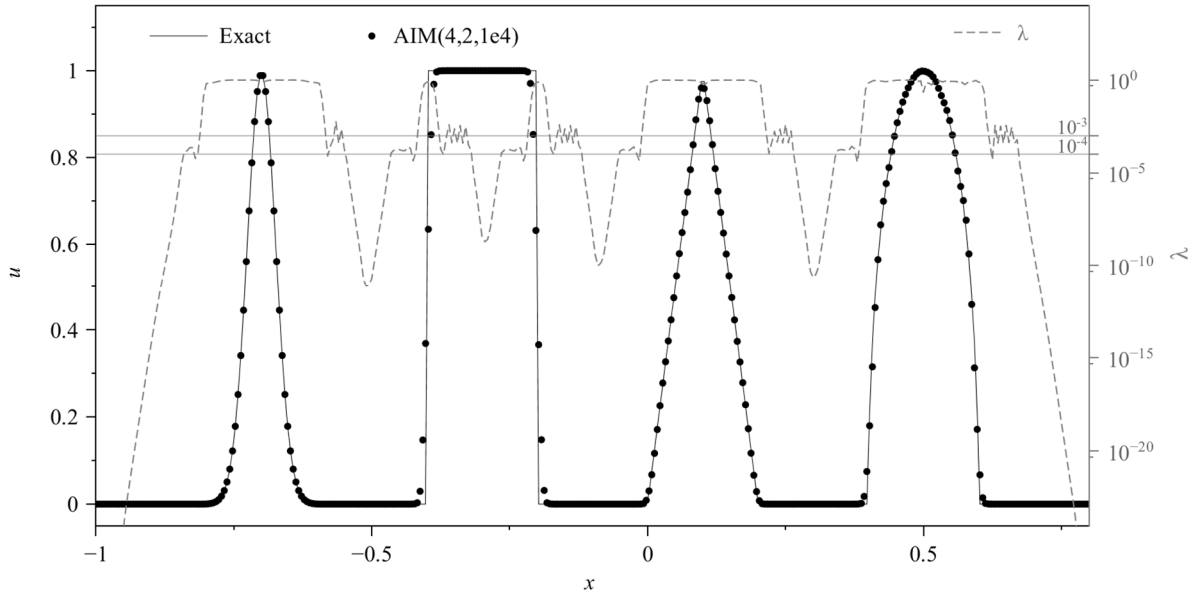

Figure 7: Results for linear advection Case 2 at $t = 2$s for $N = 400$ cells simulated using WENO-AIM(4,2,1e4) plotted together with λ (right axis)

Comparing Eqs. (28) and (29), it can be seen that the second terms in the numerator and denominator have been modified. With $s = cd^{-1}\lambda$, the ratio of the weights allocated to the most non-smooth stencils is about 0.97 which indicates that the presence of d^{-1} in the second term in the denominator removes some dependence of d in the mapping process near discontinuities. Remarkably, the results shown in Figure 6 are completely free from distortions, which suggests that the property essentially underpins the ability of WENO-AIM method to capture discontinuities accurately over long output times.

3.4 Effect of parameter λ on the mapping process

To better understand how the adaptive mapping process performs near smooth and non-smooth regions of the solution, parameter λ is plotted together with the results for linear advection Case 2 at $t = 2s$ (1 cycle) using $N = 400$ cells and $N = 800$ cells in Figures 7 and 8, respectively. Observing the results, a general pattern emerges in the variation of λ and this pattern is sketched in Figure 9. In constant region (a) to the left, λ is very small since $\max\left(IS_j\right) \ll \epsilon_m$. The small value of λ in region (a) is inconsequential since the solution remains constant and, thus, reverting to the WENO-JS scheme incurs no loss of accuracy. Moving to the right, λ increases steadily and stagnates at around 10^{-4} in region (b). In this region, the solution is truly non-smooth. Therefore, it is necessary to shrink

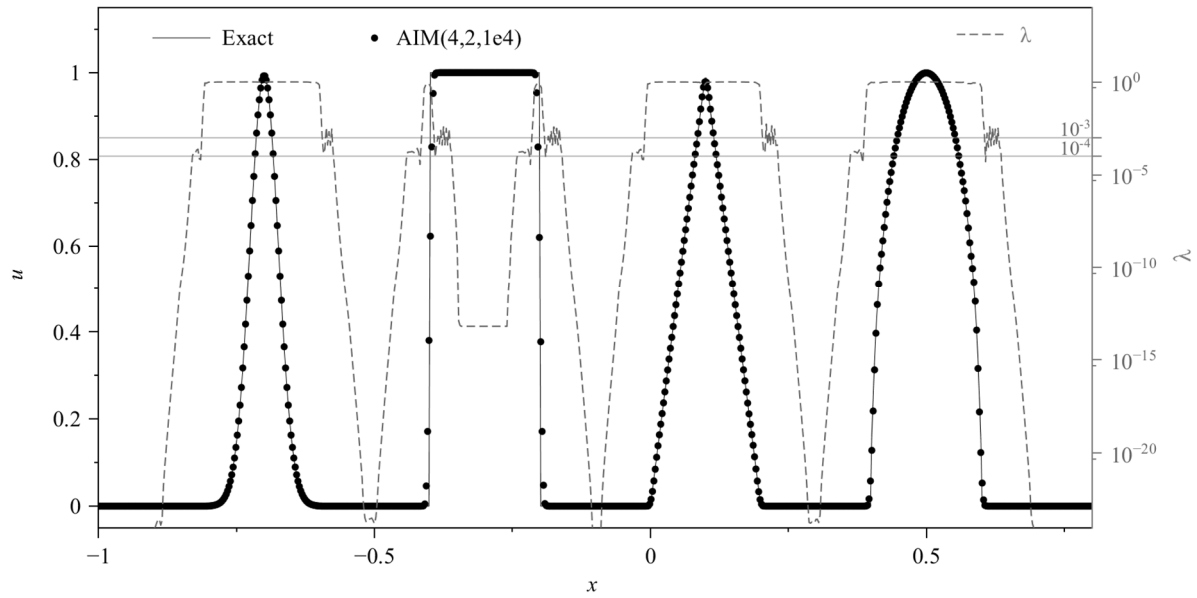

Figure 8: Results for linear advection Case 2 at t = 2s for N = 800 cells simulated using WENO-AIM(4,2,1e4) plotted together with λ (right axis)

the central range and ensure that the mapping function comes closer to the identity map. Moving further to the right, the solution becomes increasingly smooth and λ rises until it becomes nearly 1 in region (c). Notice that even the smeared discontinuities of the square wave are deemed smoothly varying. So, a large central range is maintained, and the optimal weights are applied. After crossing region (c), the solution once again becomes non-smooth causing λ to fall until it oscillates about 10^{-3} in region (d). Once again, an asymmetry is observed – non-smooth region (b) to the left of region (c) is deemed more unsmooth compared to non-smooth region (d) to its right. Upon traversing region (d), the solution approaches a constant state and λ begins to drop once again to very small values in region (e). For the finer resolution of N = 800 cells, λ becomes much smaller in the constant regions (a) and (e) compared to the coarser resolution of N = 400 cells. Nevertheless, the variation of λ in regions (b), (c) and (d) is similar at both resolutions.

3.5 Convergence properties near smooth critical points

In this section, the convergence rates r_c of the seventh order finite volume WENO-AIM(4,2,1e4) scheme with $\epsilon = 10^{-40}$ and $\epsilon_m = 0$ are compared with the convergence rates of seventh order upstream central and WENO-JS schemes for n_{cp} = 1, 2 and 3.

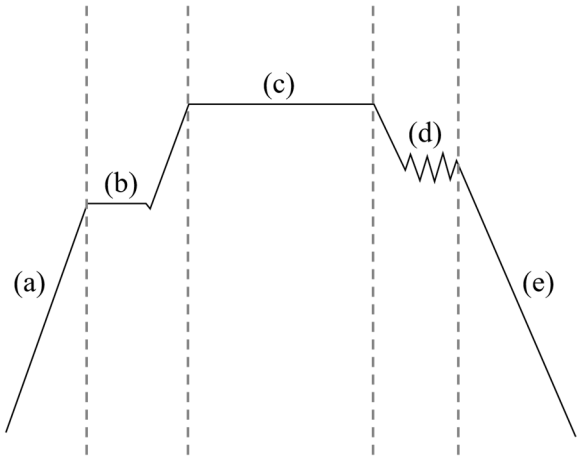

Figure 9: Sketch of the variation of λ across various regions in the solution

Consider a smooth function $f(x)$ which is averaged over seven uniform cells $[i-3,\cdots,i+3]$ of width Δx. The resultant cell averages $\left[\overline{f_{i-3}},\cdots,\overline{f_{i+3}}\right]$ can then be used to approximate the point value $f(x_{i+1/2})$. By performing this approximation at various resolutions, the convergence rate of the scheme can be determined. Henrick, et al. [7] used the smooth function $f(x)=x^3+\cos(x)$ to investigate the convergence rates of various fifth order finite difference schemes when approximating $f'(0)$. The derivatives of this function behave in the following manner.

$$f^{(k)}(0)=\begin{cases}\pm 1, & \text{if } k \text{ is even}\\ 0, & \text{if } k\neq 3 \text{ is odd}\\ 6, & \text{if } k=3\end{cases} \tag{30}$$

As evident from Eq. (30), $f(x)$ only has a $n_{cp}=1$ critical point at $x=0$. Therefore, it cannot be used to investigate the behaviour of numerical schemes near critical points of $n_{cp}\geq 2$. Secondly, since the odd order derivatives of $f(x)$ higher than third order vanish at $x=0$, finite volume schemes may converge at higher rates. For instance, since $f^{(7)}(0)=0$, the truncation error of the seventh order upstream central scheme is no longer $O(\Delta x^7)$ but $O(\Delta x^8)$ (see Eq. (7)). Therefore, the seventh order upstream central scheme actually converges at $r_c=8$ instead of the expected $r_c=7$. In order to calculate the convergence rates accurately, a different smooth function $f(x)$ of the following form is

Table 6: Convergence properties of various seventh order schemes at $n_{cp}=1$ critical point

	Upstream central		JS(1e-06)		JS(1e-40)		AIM(4,2,1e4)	
q	|error|	r_c	|error|	r_c	|error|	r_c	|error|	r_c
0	3.57163e-24	-	3.56033e-24	-	8.46082e-21	-	3.57163e-24	-
1	2.79026e-26	7.0000	2.78915e-26	6.9960	1.33063e-22	5.9906	2.76026e-26	7.0000
2	2.17986e-28	7.0000	2.17975e-28	6.9995	2.08587e-24	5.9953	2.17986e-28	7.0000
3	1.70300e-30	7.0000	1.70299e-30	7.0000	3.26445e-26	5.9977	1.70300e-30	7.0000
4	1.33047e-32	7.0000	1.33046e-32	7.0000	5.10484e-28	5.9988	1.33047e-32	7.0000

Table 7: Convergence properties of various seventh order schemes at $n_{cp}=2$ critical point

	Upstream central		JS(1e-06)		JS(1e-40)		AIM(4,2,1e4)	
q	|error|	r_c	|error|	r_c	|error|	r_c	|error|	r_c
0	3.57163e-24	-	3.57163e-24	-	8.46082e-18	-	3.57163e-24	-
1	2.79026e-26	7.0000	2.79026e-26	7.0000	1.33063e-20	5.0283	2.76026e-26	7.0000
2	2.17986e-28	7.0000	2.17986e-28	7.0000	2.08587e-21	5.0143	2.17986e-28	7.0000
3	1.70300e-30	7.0000	1.70300e-30	7.0000	3.26445e-23	5.0072	1.70300e-30	7.0000
4	1.33047e-32	7.0000	1.33047e-32	7.0000	5.10484e-24	5.0036	1.33047e-32	7.0000

Table 8: Convergence properties of various seventh order schemes at $n_{cp}=3$ critical point

	Upstream central		JS(1e-06)		JS(1e-40)		AIM(4,2,1e4)	
q	|error|	r_c	|error|	r_c	|error|	r_c	|error|	r_c
0	3.57163e-24	-	3.57163e-24	-	1.52040e-14	-	2.19614e-18	-
1	2.79026e-26	7.0000	2.79026e-26	7.0000	9.47960e-16	4.0035	1.35502e-19	4.0186
2	2.17986e-28	7.0000	2.17986e-28	7.0000	5.97160e-17	4.0017	8.41430e-21	4.0093
3	1.70300e-30	7.0000	1.70300e-30	7.0000	3.69626e-18	4.0009	5.24195e-22	4.0047
4	1.33047e-32	7.0000	1.33047e-32	7.0000	2.30946e-19	4.0004	3.27090e-23	4.0023

proposed. $f(x)$ achieves a critical point of any desired n_{cp} at $x=0$ by systematically eliminating the first n_{cp} derivatives of e^x. Furthermore, all the remaining derivatives take the particularly simple value of 1 which simplifies error analysis.

$$f(x)=e^x-\sum_{k=1}^{n_{cp}}\frac{x^k}{k!} \qquad f^{(k)}(0)=\begin{cases}0, & \text{if } k\le n_{cp}\\ 1, & \text{otherwise}\end{cases} \tag{31}$$

For each n_{cp}, the investigation was performed over five resolution levels, q = 0 to 4, where each resolution is defined as $\Delta x = 0.001/2^q$. The critical point was positioned at x_i, i.e. $x_i = 0$. The absolute errors in approximations of $f\left(x_{i+1/2}\right)$ and the convergence rates are tabulated in Tables 6-8.

Firstly, it can be observed that the upstream central scheme achieves seventh order convergence for n_{cp} up to 3. Secondly, it can be noticed that r_c drops by one with each increment in n_{cp} for WENO-JS with $\epsilon = 10^{-40}$. WENO-AIM(4,2,1e4), on the other hand, is able to maintain $r_c = 7$ up to $n_{cp} = 2$ but reverts to $r_c \approx 4$ for $n_{cp} = 3$. Notice that WENO-JS with $\epsilon = 10^{-6}$ maintains $r_c = 7$ even for $n_{cp} = 3$. This is because $\epsilon = 10^{-6} \gg \max\left(IS_j\right)$ especially for $n_{cp} > 1$ (refer to Table 1). As a result, ϵ overpowers the individual smoothness indicators IS_j in Eq. (13) causing the scheme to essentially behave like the upstream central scheme.

4 Comparison with other seventh order WENO schemes

In this section, the performance of WENO-AIM(4,2,1e4) is compared with those of other seventh order WENO methods such as WENO-JS, WENO-M, WENO-IM(2,0.1), WENO-Z and WENO-RM(260). Following the recommendations in [7, 9], ϵ was set to 10^{-40} for all schemes except WENO-JS and WENO-RM(260), for which it was set to 10^{-6} and 10^{-99}, respectively.

4.1 One dimensional linear advection

The one dimensional linear advection equation (Eq. (23)) was solved with three different initial conditions. Initial conditions for Cases 1 and 2 were given earlier in Eqs. (24) and (25), respectively. The Courant number was fixed at 0.1 for all three cases. The L_1 norms were computed using Eq. (26).

4.1.1 Case 1

Table 9: L1 error norms of seventh order WENO schemes for linear advection Case 1

Scheme	N	$t = 2$s		$t = 2000$s	
		|error|	r_c	|error|	r_c
WENO-JS	200	1.2954e-2	-	8.6231e-2	-
	400	7.0646e-3	0.8747	4.3068e-2	1.0016
	800	3.8471e-3	0.8768	2.6690e-2	0.6903
WENO-M	200	1.1029e-2	-	6.9420e-2	-
	400	6.0476e-3	0.8669	5.2326e-2	0.4078
	800	3.3521e-3	0.8513	3.9994e-2	0.3877
WENO-IM(2,0.1)	200	1.0192e-2	-	4.8390e-2	-
	400	5.6123e-2	0.8608	2.5835e-2	0.9054
	800	3.0945e-3	0.8589	1.3512e-2	0.9351
WENO-Z	200	1.0515e-2	-	2.5771e-2	-
	400	5.7570e-3	0.8690	1.4955e-2	0.7851
	800	3.1443e-3	0.8726	9.2878e-3	0.6872
WENO-RM(260)	200	1.0625e-2	-	2.9235e-2	-
	400	5.8023e-3	0.8728	1.6048e-2	0.8653
	800	3.1678e-3	0.8731	8.7061e-3	0.8823
WENO-AIM(4,2,1e4)	200	9.9609e-3	-	2.5303e-2	-
	400	5.4925e-3	0.8588	1.3975e-2	0.8565
	800	3.0206e-3	0.8626	7.7513e-3	0.8504

The L_1 error norms linear advection Case 1 are given in Table 9 for $N = 200$, 400 and 800 cells at $t = 2s$ (1 cycle) and $t = 2000s$ (1000 cycles). It is very clear that WENO-AIM(4,2,1e4) outperforms all other schemes over short and long output times regardless of the mesh resolutions. Between the other schemes, WENO-IM(2,0.1) performs the best at short output time but its errors diverge quickly and incurs nearly twice the errors incurred by WENO-AIM(4,2,1e4) over long output times. This situation does not improve with increasing resolution. It is also evident from the results that WENO-JS has the highest starting error among all the schemes but WENO-M results in the poorest performance at long output times even at higher resolutions. Therefore, it is not recommended to use seventh order WENO-M scheme. WENO-Z performs better than WENO-RM(260) for this case at both short and long output times.

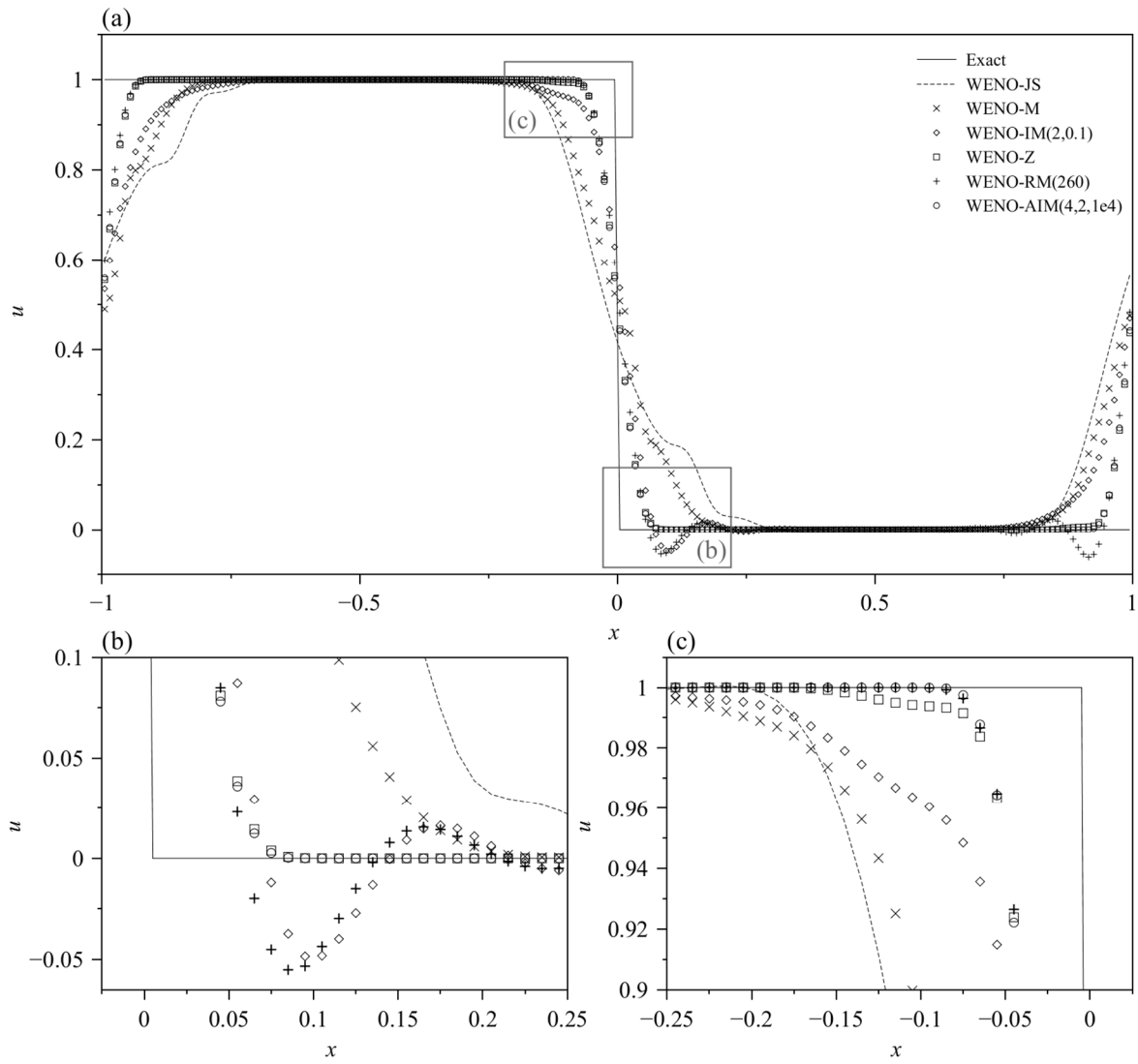

Figure 10: Performance of seventh order WENO methods for linear advection Case 1 using $N = 200$ cells at $t = 2000s$.

The results for $N = 200$ cells at $t = 2000s$ (1000 cycles) are plotted in Figure 10. It can be observed that WENO-JS, WENO-M and WENO-IM(2,0.1) result in severe distortions near the discontinuities. With the exception of WENO-AIM(4,2,1e4), a general asymmetry can be observed in the performance of all other schemes. For instance, WENO-RM(260) performs well upstream of the smeared discontinuity (Figure 10(c)) but produces spurious oscillations downstream (Figure 10(b)). On the other hand, WENO-Z which rivals the performance of WENO-AIM(4,2,1e4) downstream of the discontinuity (Figure 10(b)) results in a slightly distorted profile upstream (Figure 10(c)).

WENO-IM(2,0.1) and WENO-RM(260) are the only schemes to produce spurious oscillations. While it comes as no surprise that WENO-IM(2,0.1) produces spurious oscillations due to excessive

Table 10: L1 error norms of seventh order WENO schemes for linear advection Case 2

Scheme	N	$t = 2$s		$t = 2000$s	
		|error|	r_c	|error|	r_c
WENO-JS	200	1.9840e-2	-	2.2130e-1	-
	400	9.2835e-3	1.0957	1.4184e-1	0.6417
	800	4.6420e-3	0.9999	4.3117e-2	1.7180
WENO-M	200	1.6579e-2	-	2.1705e-1	-
	400	8.1281e-3	1.0283	1.2854e-1	0.7558
	800	4.1373e-3	0.9742	8.7545e-2	0.5541
WENO-IM(2,0.1)	200	1.5367e-2	-	1.1342e-1	-
	400	7.5215e-3	1.0307	4.7536e-2	1.2546
	800	3.8007e-3	0.9848	2.0224e-2	1.2330
WENO-Z	200	1.5896e-2	-	6.2709e-2	-
	400	7.6801e-3	1.0494	2.9208e-2	1.1023
	800	3.8380e-3	1.0001	1.3861e-2	1.0754
WENO-RM(260)	200	1.6082e-2	-	5.7005e-2	-
	400	7.7771e-3	1.0482	2.5953e-2	1.1352
	800	3.8772e-3	1.0042	1.2461e-2	1.0585
WENO-AIM(4,2,1e4)	200	1.5034e-2	-	5.8376e-2	-
	400	7.3580e-3	1.0308	2.5271e-2	1.2079
	800	3.6969e-3	0.9930	1.1013e-2	1.1983

amplification of the weights of non-smooth stencils, it is definitely curious that WENO-RM(260) which has been designed to actively suppress the weights of non-smooth stencils results in a similar behaviour.

4.1.2 Case 2

The L_1 error norms linear advection Case 2 are given in Table 10 for $N = 200$, 400 and 800 cells at $t = 2s$ (1 cycle) and $t = 2000s$ (1000 cycles). A short output times, WENO-AIM(4,2,1e4) outperforms all other seventh order schemes followed by WENO-IM(2.0,1), WENO-Z and then WENO-RM(260). WENO-JS and WENO-M do not perform as well as the other schemes at both short and long output times. At long output times, the performance of WENO-IM(2,0.1) deteriorates significantly. These trends are consistent with the results from Case 1 but some differences exist. For Case 2,

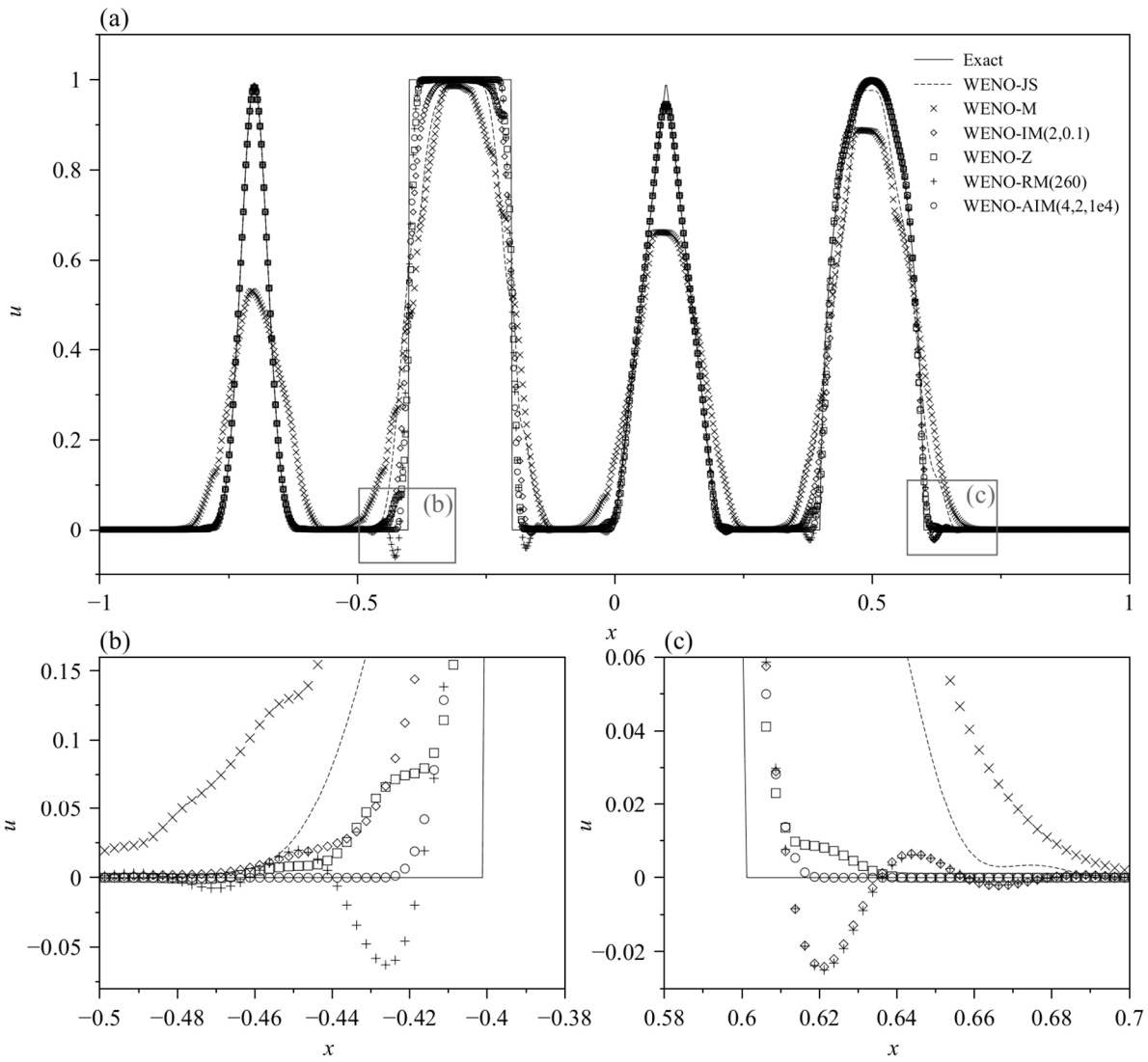

Figure 11: Performance of seventh order WENO methods for linear advection Case 2 using $N = 800$ cells at $t = 2000s$.

WENO-RM(260) performs better than WENO-Z at long output times. In fact, WENO-RM(260) delivers excellent performance at long output times when using $N = 200$ cells which is closely followed behind by WENO-AIM(4,2,1e4). However, WENO-AIM(4,2,1e4) produces the smallest errors at the finer resolutions of $N = 400$ and 800 cells.

The results for $N = 800$ cells at $t = 2000s$ (1000 cycles) is plotted in Figure 11. With the exception of WENO-M, all the other schemes deliver comparable performances in capturing the Gaussian and triangle waves including WENO-JS. The performances of the schemes differ the most for the square wave and at the foot of the profiles where the solution changes from a constant state to a non-smooth region or vice versa. At these critical regions, the performances of the schemes are highly reminiscent

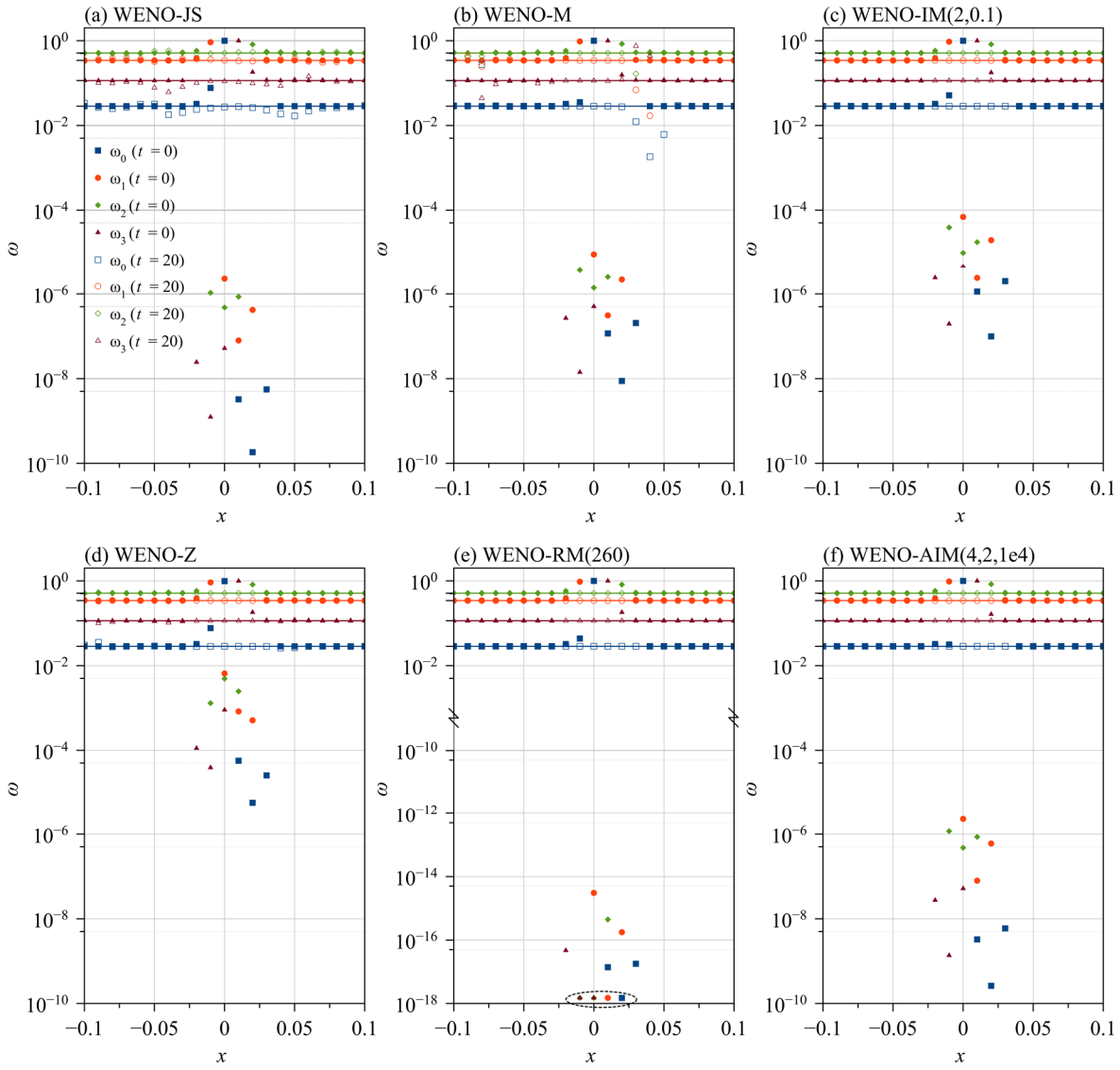

Figure 12: Non-linear weights of seventh order WENO schemes for linear advection Case 3 for $t = 0s$ (solid symbols) and $t = 20s$ (empty symbols). Optimal weights are marked by horizontal lines.

of those for case 1. Once again, it can be noticed that WENO-IM(2,0.1) and WENO-RM(260) are the only schemes to produce spurious oscillations. Only WENO-AIM(4,2,1e4) is able to maintain an oscillation- and distortion-free profile over long output times.

4.1.3 Case 3

The initial condition for Case 3 is given in Eq. (32). The profile consists of two smooth regions separated by a discontinuity at $x = 0$. Borges, et al. [12] used this test case to compare the weights allocated to the stencils near the discontinuity. A similar comparison will be performed next. The case

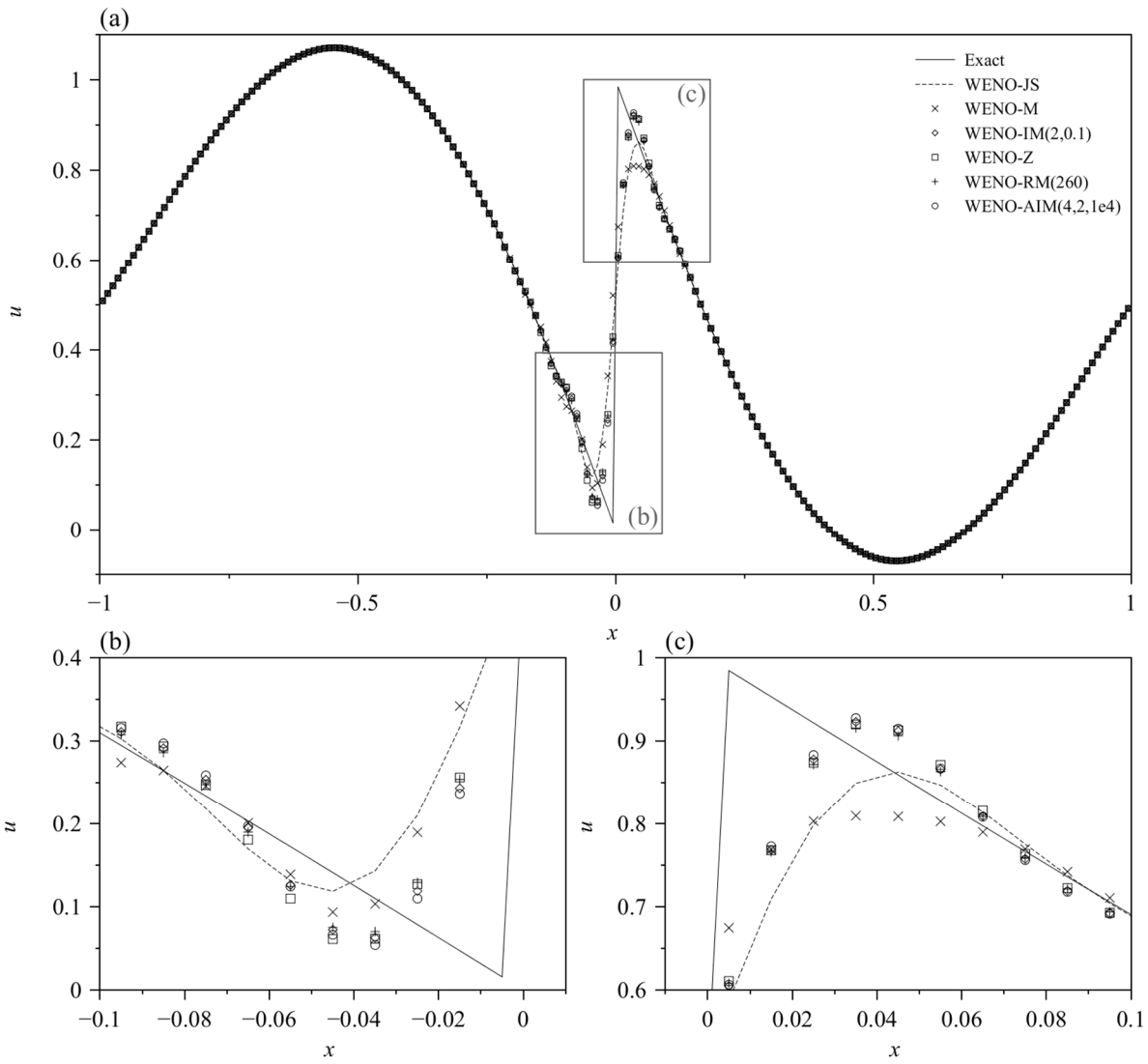

Figure 13: Performance of seventh order WENO methods for linear advection Case 3 using $N = 200$ cells at $t = 20s$.

was solved on the domain $x \in [-1, 1]$ discretized into $N = 200$ cells. The simulation was run until $t = 20s$ (10 cycles). The non-linear weights ω_j at $t = 0s$ and $t = 20s$ are shown in Figure 12.

$$u_0(x) = \begin{cases} -\sin(\pi x) - \frac{1}{2}x^3 & -1 < x < 0 \\ -\sin(\pi x) - \frac{1}{2}x^3 + 1 & 0 \le x \le 1 \end{cases} \tag{32}$$

As expected, all methods allocate small weights to sub-stencils containing the discontinuity at the start of the simulation. Among them, WENO-RM(260) assigns the smallest weights to the non-smooth sub-stencils. In fact, some of the weights computed by WENO-RM(260) were zero or even negative due to numerical errors which have been circled in Figure 12(e). Conversely, WENO-Z assigns the

greatest weights to sub-stencils containing the discontinuity followed by WENO-IM(2,0.1) and WENO-M. More importantly, the weights allocated to the non-smooth sub-stencils by WENO-AIM(4,2,1e4) at $t = 0s$ are comparable to those assigned by WENO-JS.

At the end of 10 cycles, the non-linear weights of WENO-Z, WENO-IM(2,0.1), WENO-RM(260) and WENO-AIM(4,2,1e4) become almost coincident with the optimal weights, i.e. $\widetilde{\omega_j} \approx d_j$. The initial discontinuity has been smeared/smoothened sufficiently to allow the entire profile to be captured using the upstream central scheme. In contrast, the non-linear weights of WENO-JS still deviate from the optimal weights on either side of the smeared discontinuity. Inspecting the results near the discontinuity at the end of 10 cycles (Figure 13), it appears that the deviations correspond to the two critical points that develop on either side of the smeared discontinuity. WENO-M also exhibits severe deviations from the optimal weights but only on the right side of the discontinuity; the non-linear weights approach the optimal weights on the left. Correspondingly, WENO-M performs much better on the left side of the discontinuity where the mapped weights are close to the optimal weights; on the right, the weights deviate more severely from the optimal weights. Lastly, close examination of Figure 13(b) and (c) reveals that WENO-AIM(4,2,1e4) results in the highest peak among all the schemes.

4.2 Euler equations

Consider the two-dimensional Euler equations given below in split form oriented in the *n*-direction that is normal to a cell interface. Here ρ, u, v, p, e and h refer to the gas density, face normal velocity, tangential velocity, pressure, specific total energy and specific total enthalpy. γ is the ratio of specific heats with a value of 1.4.

$$\partial_t \mathbf{U} + \partial_n \mathbf{F}(\mathbf{U}) = 0 \quad \text{where} \quad \mathbf{U} = \begin{pmatrix} \rho \\ \rho u \\ \rho v \\ \rho e \end{pmatrix}, \mathbf{F} = \begin{bmatrix} \rho u \\ \rho u^2 + p \\ \rho v u \\ \rho h u \end{bmatrix}, e = \frac{p}{(\gamma - 1)\rho} + \frac{u^2 + v^2}{2} \quad \text{and} \quad h = e + \frac{p}{\rho} \tag{33}$$

For high order spatial schemes, it is well known that a characteristic flux approach is necessary to prevent the formation of spurious oscillations [16]. In this study, the characteristic flux computation

based on Rusanov flux described in Ref. [17] was implemented. The computation of characteristic fluxes requires an expensive local characteristic decomposition to be performed at each cell interface. While the computational cost of running a fully characteristic solver is reasonable for one-dimensional problems, it becomes prohibitively expensive for higher dimensional problems. Therefore, a hybrid solver was used for the two-dimensional case. The hybrid solver applies the HLLC flux scheme [18] computed using a MUSCL approach by interpolating the state variables $\mathbf{V} = (\rho, \rho u, \rho v, p)$ at all cell interfaces except in the vicinity of shocks where it applies the Rusanov-based characteristic flux scheme.

4.2.1 Definition of λ for Euler equations

It was observed that for certain cases, WENO-AIM(4,2,1e4) became unstable within a few time steps of the commencement of the simulation. The double Mach reflection problem (Case 6) was one such case. This was quite surprising since WENO-AIM(4,2,1e4) is designed to revert to WENO-JS scheme near discontinuities and WENO-JS scheme itself remains stable for such cases. The only explanation is that WENO-AIM(4,2,1e4) does not reduce to the WENO-JS fast enough. Therefore, to stabilize the adaptive mapping method, the parameter λ was taken to the minimum over the left- and right-biased stencils, i.e. $\lambda = \min(\lambda_L, \lambda_R)$, and this common λ was used for both sided interpolations. The intuition behind this idea is that, unlike the linear advection cases where only a left-biased interpolation is required, both left- and right-biased interpolations are required for the Euler equations. In other words, both left- and right-biased stencils have an effect on the computation of the numerical flux. So, it is only natural that the adaptive parameter λ depends on both stencils. For most cases, λ_L and λ_R do not differ much and, thus, this treatment is not always necessary. In fact, most cases were able to run in a stable manner without this treatment. Nevertheless, all the cases to be presented next were simulated using this definition for consistency.

4.2.2 Case 4: Sod's problem

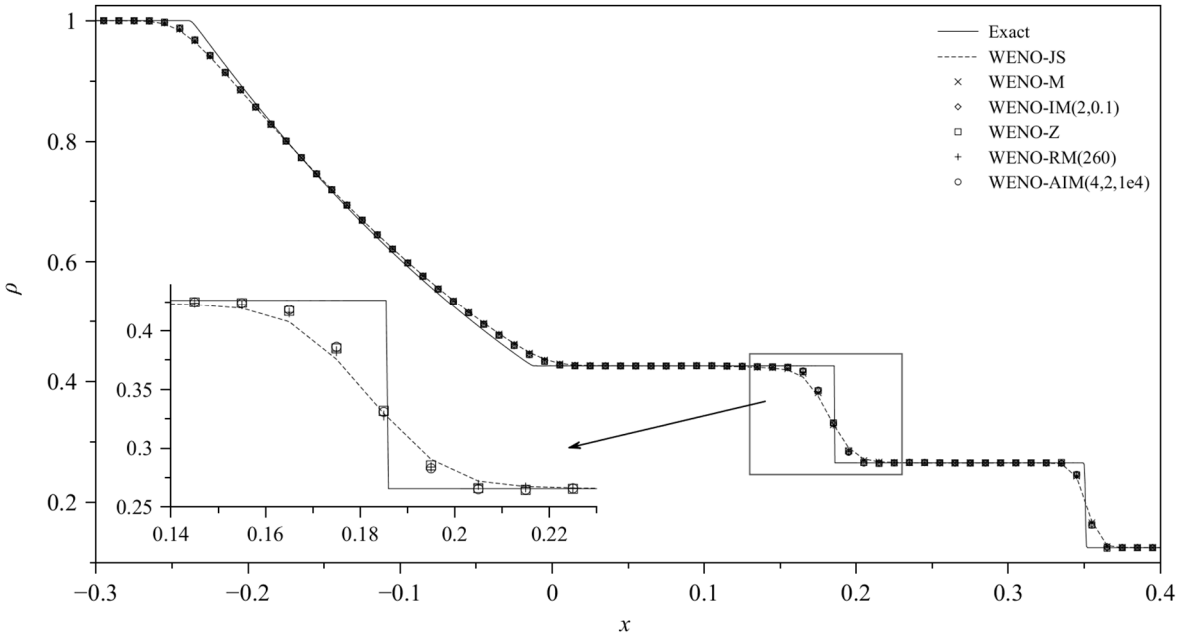

Figure 14: Performance of seventh order WENO schemes for Case 4 using $N = 100$ cells. Results are shown at $t = 0.2s$.

The initial conditions for Sod's problem [19] is given in Eq. (34). This classic case is a test of the numerical scheme's ability to capture the sharp changes across the shock and contact discontinuity without excessive numerical diffusion or spurious oscillations. The simulation was performed on the domain $x \in [-0.5, 0.5]$ discretized into $N = 100$ uniform cells with Dirichlet boundaries till $t = 0.2s$.

Case 4

$$(\rho, u, p)_0 = \begin{cases} (0.125, 0, 0.1) & -0.5 \le x \le 0 \\ (1.000, 0, 1.0) & 0 < x \le 0.5 \end{cases} \tag{34}$$

The initial conditions consist of stationary gas of different pressures and density. Upon initialization, a shock wave propagates to the right followed by a contact discontinuity while an expansion fan propagates to the left. The final density profiles are shown in Figure 14.

It can be seen from the results that all the mapped WENO schemes and WENO-Z perform better than the WENO-JS scheme at the contact discontinuity and shock. Close examination shows that WENO-AIM(4,2,1e4) captures a slightly sharper contact discontinuity compared to WENO-Z and WENO-RM(260) schemes.

4.2.3 Case 5: Shock-entropy wave interaction problems

Two cases of shock-entropy wave interaction problems were tested. Cases (a) and (b) are sometimes referred to in the literature as the Shu-Osher problem [20] and Titarev-Toro problem [21], respectively. These cases test the numerical scheme's ability to capture both shocks and short wavelength oscillations. The amplitudes of the short wavelength oscillations are a measure of the numerical viscosity of the scheme. The initial conditions for the two cases are given in Eq. (35) and Eq. (36). Both cases were simulated on the domain $x \in [-5, 5]$ with Dirichlet boundaries. Case 5(a) was run with $N = 200$ uniform cells till $t = 1.8s$ while Case 5(b) was run with $N = 1000$ uniform cells till $t = 5s$.

Case 5(a)
$$(\rho, u, p) = \begin{cases} (3.857143, 2.629369, 10.33333) & -5 \le x < -4 \\ (1 + 0.2\sin(5x), 0, 1) & -4 \le x < 5 \end{cases} \tag{35}$$

Case 5(b)
$$(\rho, u, p) = \begin{cases} (1.515695, 0.523346, 1.80500) & -5 \le x < -4.5 \\ (1 + 0.1\sin(20x), 0, 1) & -4.5 \le x < 5 \end{cases} \tag{36}$$

The initial conditions involve a shock wave propagating to the right towards a stationary region of sinusoidal density variations. As the shock interacts with the sinusoidal density variations, short wavelength high amplitude density waves are produced behind the shock. These waves are followed by a sequence of long wavelength low amplitude waves which steepen over time into N-waves. Case 5(b) is a more severe version of 5(a); it produces waves of shorter wavelength compared to Case 5(a). The final density profiles for Cases 5(a) and (b) are shown in Figure 15 and Figure 16, respectively. The reference solution for Case 5(a) was computed on a 2000-cell grid while that of Case 5(b) was computed on a 10000-cell grid. Both reference solutions were computed using seventh order WENO-JS scheme.

For Case 5(a), it is clear from the results in Figure 15 that WENO-JS is the most dissipative of the schemes. WENO-AIM(4,2,1e4) produces the largest amplitudes of the short wavelength oscillations among all the schemes. Among the other mapped WENO schemes, WENO-IM(2,0.1) produces the highest amplitudes followed by WENO-RM(260) and WENO-M. The performance of WENO-Z is comparable performance to that of WENO-M.

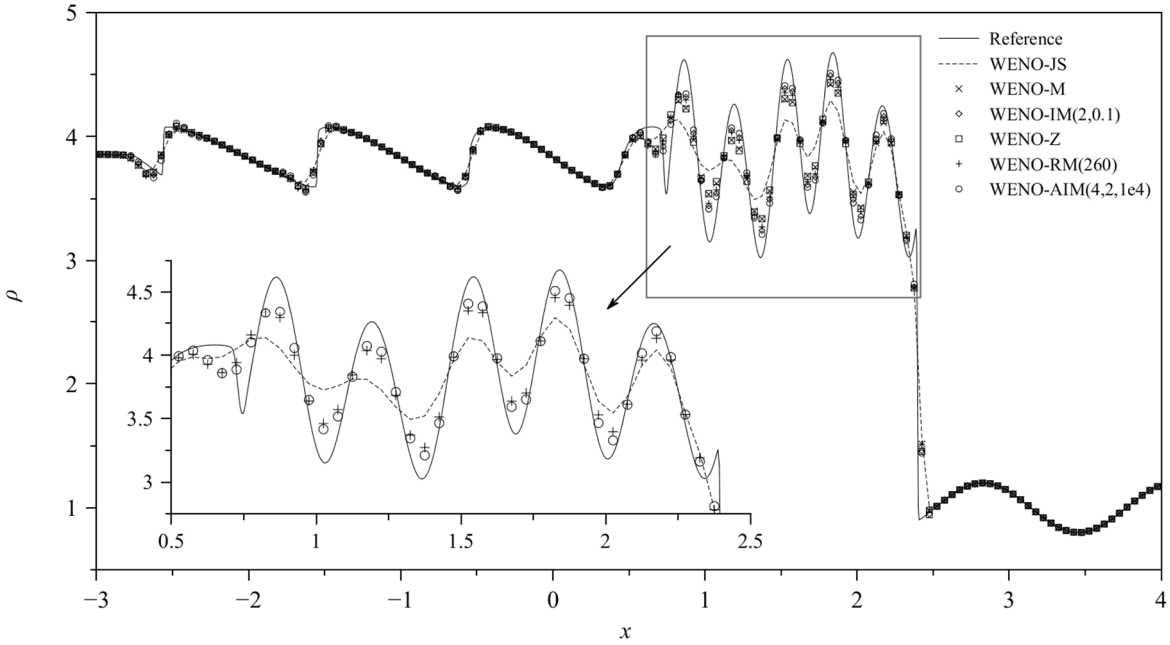

Figure 15: Performance of seventh order WENO schemes for Case 5(a) using $N = 200$ cells. Results are shown at $t = 1.8s$.

For Case 5(b), it had been shown by Wang, et al. [10] that WENO-RM(260) produces the highest amplitudes for the short wavelength oscillations compared to WENO-M and WENO-IM(2,0.1). It can be seen from Figure 16(b) that WENO-AIM(4,2,1e4) results in slightly greater amplitudes compared to WENO-RM(260). Surprisingly, WENO-Z was found to perform worse than all the mapped WENO methods for this case.

4.2.4 Case 6: Double Mach reflection problem

The double Mach reflection problem is a two dimensional problem that was introduced by Woodward and Colella [22] in which a strong oblique shock impinges on a ramp to produce an intricate flow structure involving multiple shock reflections and slip lines. The simulation was performed on the domain $x \times y \in [-1, 3] \times [0, 1]$ discretized uniformly into cells of width $\Delta x = \Delta y = 1/240$. The problem was initialized with a Mach 10 oblique shock oriented at an angle of θ to the horizontal axis passing through the point $(x_s, 0)$ as shown in Eq. (37).

$$\textit{Case 6} \qquad (\rho, u, v, p)_0 = \begin{cases} (8.0, -8.25\cos\theta, 8.25\sin\theta, 116.5), & y \geq (x - x_s)\tan\theta \\ (1.4, 0, 0, 1.0), & y < (x - x_s)\tan\theta \end{cases} \tag{37}$$

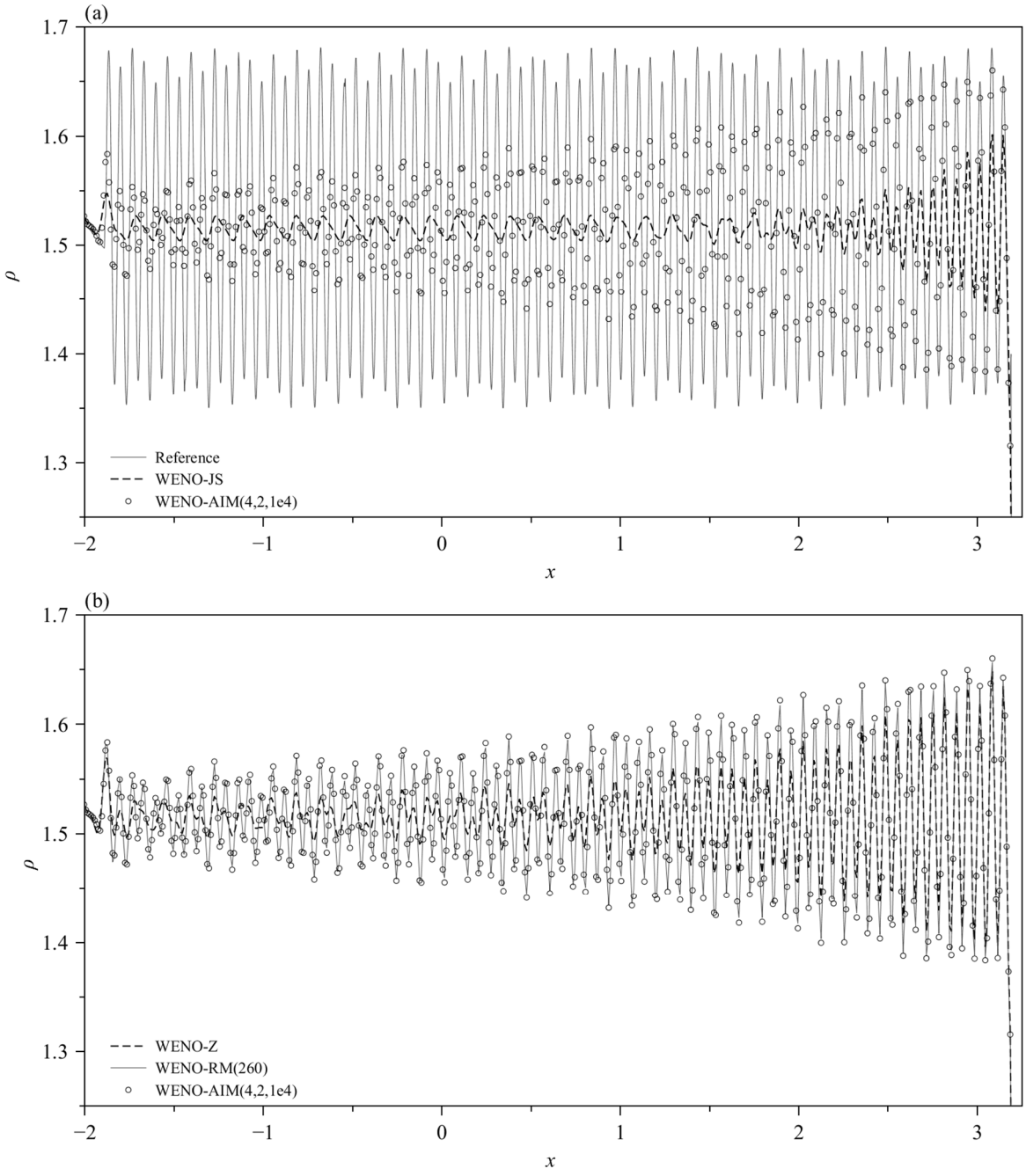

Figure 16: Performance of seventh order WENO schemes for Case 5(b) using $N = 1000$ cells. Results are shown at $t = 5s$.

Exact post-shock values were prescribed along the left boundary while Neumann boundary condition was prescribed along the right. Reflective boundary condition was applied along the bottom boundary $x \in [0, 3]$ to represent the ramp. In this study, the simulation was performed using an alternative setup that was proposed by the authors in Ref. [23]. Instead of starting with the shock situated at the foot of the ramp $x_s = 0$ as suggested in the original setup, the shock was initialized a short distance to the left

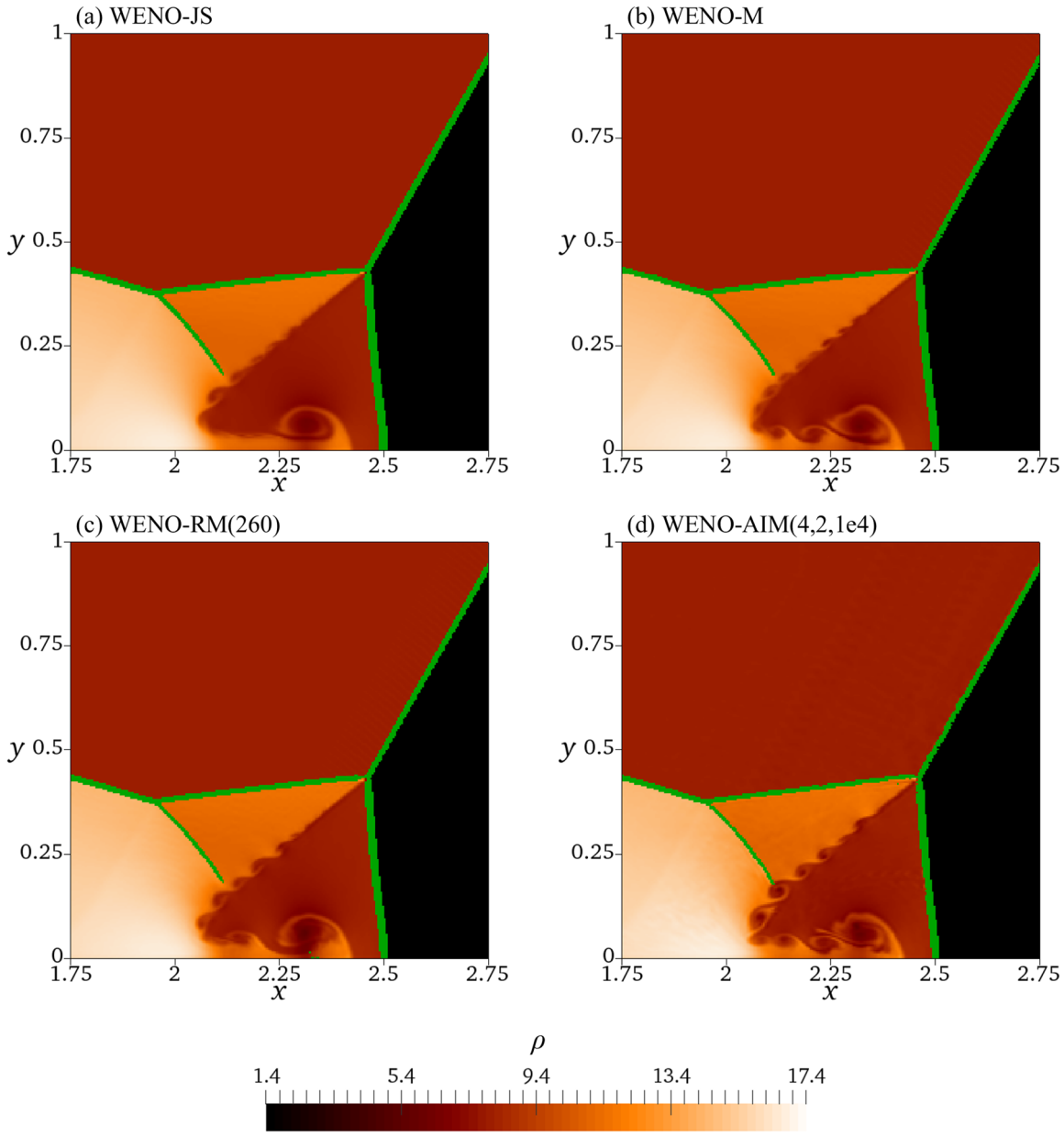

Figure 17: Close-up views of performance of seventh order WENO schemes for Case 6. Results are shown at $t = 0.27s$. Regions where characteristic flux scheme was applied is coloured green.

of the ramp at $x_s = -0.9$ and allowed to propagate until it reaches the ramp at $t_1 = 0.08s$. In addition, unlike in the original setup where $\theta = 60°$, $\theta = \tan^{-1}(7/4) \approx 60.25°$ was used because it greatly simplifies the boundary treatment at the upper boundary and the portion of the lower boundary to the left of the ramp. At t_1, the region behind the shock is re-initialized with the post-shock values in order to eliminate numerical noise which would otherwise corrupt the numerical solution and the simulation is then run till $t_2 = 0.27s$.

Both WENO-Z and WENO-IM(2,0.1) schemes became unstable within the first few time steps. As mentioned earlier, a common λ was essential for the stability of WENO-AIM(4,2,1e4) for this case. All other schemes were able to run till completion. The close-up views of the roll-ups that occur along the slip line are shown in Figure 17. The regions where characteristic flux scheme was applied is highlighted in green. It can be observed from the results that WENO-AIM(4,2,1e4) captures larger and more well-defined roll-ups compared to the other schemes. WENO-JS produces small and very diffused roll-ups, especially along the wall-attached jet. While WENO-M and WENO-RM(260) are able to capture the roll-ups on the jet, the size and definition of the roll-ups are comparable to those obtained using WENO-JS.

5 Conclusions

It was shown through Taylor series analysis that the seventh order finite volume WENO-JS scheme suffers from a loss of accuracy near critical points. While the mapped WENO methods WENO-M and WENO-IM(2,0.1) are able to recover the optimal order near critical points, they do not perform well for seventh order schemes. Based on the vastly superior performance of WENO-IM(2,0.1) over WENO-M for fifth order schemes, it became clear that using weights close to the optimal weights, not only at critical points, but more importantly in smooth regions with small derivatives, is crucial. Therefore, it was hypothesized that a large central range might be the key to achieve better results at seventh order. However, widening the central range increases the risk of amplifying the weights of non-smooth sub-stencils resulting in spurious oscillations.

To this end, a general class of rational mapping functions [11] has been introduced with a parameter λ to create the adaptive improved mapping method, WENO-AIM. The rational mapping functions have the beneficial property of having unit slope, i.e. $g'_{\mathrm{RM}}(0)=1$, for $m>1$ which ensures that near-zero weights do not get amplified. The parameter λ senses the local smoothness of the solution by making use of the information available in the smoothness indicators and tailors the mapping function accordingly. After a parametric study, it was concluded that WENO-AIM(4,2,1e4) delivers very good

performance for different cases and was able to recover the optimal order of accuracy near critical points up to $n_{cp} = 2$.

The performance of WENO-AIM(4,2,1e4) was compared with the original WENO-JS scheme and other enhanced seventh order WENO schemes such as WENO-M, WENO-IM(2,0.1), WENO-RM(260) and WENO-Z. It was demonstrated that WENO-AIM(4,2,1e4) performs the best for linear advection cases over short and long output times. WENO-AIM(4,2,1e4) was also found to perform better than the other schemes for Euler equations.

Finally, it should be remarked that although the results are not presented in this paper, a similar comparison for fifth order schemes was performed for both the linear advection and Euler equations cases. For linear advection cases, WENO-AIM(4,2,1e4) performed the best at short output times. Even though WENO-IM(2,0.1) resulted in smaller errors than WENO-RM(260) over long output times for Case 1, it resulted in tiny asymmetric distortions near the discontinuities. For Case 2, WENO-RM(260) delivered the better overall performance at long output times closely followed by WENO-AIM(4,2,1e4). For Sod's shock tube problem (Case 4) and both shock-entropy wave interaction problems (Cases 5(a) and (b)), WENO-AIM(4,2,1e4) again delivered the best performance followed by WENO-IM(2,0.1) and WENO-RM(260).

Hence, mapped WENO approach represents an important step towards the improvement of WENO schemes. The adaptive mapping approach introduced in this paper takes yet another step towards this goal. With a suitable choice of parameters, adapting mapping could improve the performance of higher order WENO methods significantly while maintaining stability.

6 Appendix A

The objective of this section is to derive the explicit forms of IS_j for the seventh order finite volume WENO scheme.

Each sub-stencil j of the seventh order WENO results in a third order polynomial $p_j(x) = \sum_{n=0}^{3} b_{jn} x^n$ and a corresponding smoothness indicator IS_j computed as shown in Eq. (14). Without loss of generality, consider the simple case where $\Delta x = 1$ and $x_i = 0$. The expression for IS_j simplifies to the following.

$$
\begin{aligned}
IS_j &= \sum_{k=1}^{3} \int_{x_i-\Delta x/2}^{x_i+\Delta x/2} \Delta x^{2k-1} \left[\frac{d^k p_j(x)}{dx^k} \right]^2 dx \\
&= \sum_{k=1}^{3} \int_{-1/2}^{+1/2} \left[\frac{d^k p_j(x)}{dx^k} \right]^2 dx \\
&= \sum_{k=1}^{3} \int_{-1/2}^{+1/2} \left[\frac{d^k}{dx^k} \left(b_{j0} + b_{j1}x + b_{j2}x^2 + b_{j3}x^3 \right) \right]^2 dx \\
&= \int_{-1/2}^{+1/2} \left(b_{j1} + 2b_{j2}x + 3b_{j3}x^2 \right)^2 + \left(2b_{j2} + 6b_{j3}x \right)^2 + \left(6b_{j3} \right)^2 dx \\
&= b_{j1}^2 + \frac{1}{2} b_{j1} b_{j3} + \frac{13}{3} b_{j2}^2 + \frac{3129}{80} b_{j3}^2 \\
&= \left(b_{j1} + \frac{1}{4} b_{j3} \right)^2 + \frac{13}{3} b_{j2}^2 + \frac{781}{20} b_{j3}^2
\end{aligned}
$$

Averaging $p(x)$ over the k^{th} cell using the following formula results in a general expression for the cell average $\overline{u_k}$ in terms of the coefficients b_{jn}.

$$
\begin{aligned}
\overline{u_k} &= \frac{1}{\Delta x} \int_{x_k-\Delta x/2}^{x_k+\Delta x/2} p(x)\, dx \\
&= \int_{(k-i)-1/2}^{(k-i)+1/2} \left[b_{j0} + b_{j1}x + b_{j2}x^2 + b_{j3}x^3 \right] dx \\
&= b_{j0} + (k-i) b_{j1} + \left[(k-i)^2 + \frac{1}{12} \right] b_{j2} + \left[(k-i)^3 + \frac{1}{4}(k-i) \right] b_{j3}
\end{aligned}
$$

For each sub-stencil j, a linear system of equations can be formed from the above expression which can be solved to obtain the coefficients b_{jn} in terms of the cell averages $\overline{u_k}$. Substituting the coefficients b_{jn} into the succinct form of IS_j derived earlier yields the explicit forms of IS_j in terms of the cell averages. This procedure is shown below for each of the sub-stencils.

<u>*j*=0</u>

$$\begin{bmatrix} 1 & -3 & 109/12 & -111/4 \\ 1 & -2 & 49/12 & -17/2 \\ 1 & -1 & 13/12 & -5/4 \\ 1 & 0 & 1/12 & 0 \end{bmatrix} \begin{Bmatrix} b_{00} \\ b_{01} \\ b_{02} \\ b_{03} \end{Bmatrix} = \begin{Bmatrix} \overline{u_{i-3}} \\ \overline{u_{i-2}} \\ \overline{u_{i-1}} \\ \overline{u_i} \end{Bmatrix} \rightarrow \begin{Bmatrix} b_{00} \\ b_{01} \\ b_{02} \\ b_{03} \end{Bmatrix} = \begin{bmatrix} 1/24 & -1/6 & 5/24 & 11/12 \\ -7/24 & 11/8 & -23/8 & 43/24 \\ -1/2 & 2 & -5/2 & 1 \\ -1/6 & 1/2 & -1/2 & 1/6 \end{bmatrix} \begin{Bmatrix} \overline{u_{i-3}} \\ \overline{u_{i-2}} \\ \overline{u_{i-1}} \\ \overline{u_i} \end{Bmatrix}$$

$$IS_0 = \left(b_{01} + \frac{1}{4} b_{03} \right)^2 + \frac{13}{3} b_{02}^2 + \frac{781}{20} b_{03}^2$$

$$= \left(\begin{bmatrix} -1/3 \\ 3/2 \\ -3 \\ 11/6 \end{bmatrix}^T \cdot \begin{Bmatrix} \overline{u_{i-3}} \\ \overline{u_{i-2}} \\ \overline{u_{i-1}} \\ \overline{u_i} \end{Bmatrix} \right)^2 + \frac{13}{3} \left(\begin{bmatrix} -1/2 \\ 2 \\ -5/2 \\ 1 \end{bmatrix}^T \cdot \begin{Bmatrix} \overline{u_{i-3}} \\ \overline{u_{i-2}} \\ \overline{u_{i-1}} \\ \overline{u_i} \end{Bmatrix} \right)^2 + \frac{781}{20} \left(\begin{bmatrix} -1/6 \\ 1/2 \\ -1/2 \\ 1/6 \end{bmatrix}^T \cdot \begin{Bmatrix} \overline{u_{i-3}} \\ \overline{u_{i-2}} \\ \overline{u_{i-1}} \\ \overline{u_i} \end{Bmatrix} \right)^2$$

<u>*j*=1</u>

$$\begin{bmatrix} 1 & -2 & 49/12 & -17/2 \\ 1 & -1 & 13/12 & -5/4 \\ 1 & 0 & 1/12 & 0 \\ 1 & 1 & 13/12 & 5/4 \end{bmatrix} \begin{Bmatrix} b_{10} \\ b_{11} \\ b_{12} \\ b_{13} \end{Bmatrix} = \begin{Bmatrix} \overline{u_{i-2}} \\ \overline{u_{i-1}} \\ \overline{u_i} \\ \overline{u_{i+1}} \end{Bmatrix} \rightarrow \begin{Bmatrix} b_{10} \\ b_{11} \\ b_{12} \\ b_{13} \end{Bmatrix} = \begin{bmatrix} 0 & -1/24 & 13/12 & -1/24 \\ 5/24 & -9/8 & 5/8 & 7/24 \\ 0 & 1/2 & -1 & 1/2 \\ -1/6 & 1/2 & -1/2 & 1/6 \end{bmatrix} \begin{Bmatrix} \overline{u_{i-2}} \\ \overline{u_{i-1}} \\ \overline{u_i} \\ \overline{u_{i+1}} \end{Bmatrix}$$

$$IS_1 = \left(b_{11} + \frac{1}{4} b_{13} \right)^2 + \frac{13}{3} b_{12}^2 + \frac{781}{20} b_{13}^2$$

$$= \left(\begin{bmatrix} 1/6 \\ -1 \\ 1/2 \\ 1/3 \end{bmatrix}^T \cdot \begin{Bmatrix} \overline{u_{i-2}} \\ \overline{u_{i-1}} \\ \overline{u_i} \\ \overline{u_{i+1}} \end{Bmatrix} \right)^2 + \frac{13}{3} \left(\begin{bmatrix} 0 \\ 1/2 \\ -1 \\ 1/2 \end{bmatrix}^T \cdot \begin{Bmatrix} \overline{u_{i-2}} \\ \overline{u_{i-1}} \\ \overline{u_i} \\ \overline{u_{i+1}} \end{Bmatrix} \right)^2 + \frac{781}{20} \left(\begin{bmatrix} -1/6 \\ 1/2 \\ -1/2 \\ 1/6 \end{bmatrix}^T \cdot \begin{Bmatrix} \overline{u_{i-2}} \\ \overline{u_{i-1}} \\ \overline{u_i} \\ \overline{u_{i+1}} \end{Bmatrix} \right)^2$$

i=2

$$\begin{bmatrix} 1 & -1 & 13/12 & -5/4 \\ 1 & 0 & 1/12 & 0 \\ 1 & 1 & 13/12 & 5/4 \\ 1 & 2 & 49/12 & 17/2 \end{bmatrix} \begin{Bmatrix} b_{20} \\ b_{21} \\ b_{22} \\ b_{23} \end{Bmatrix} = \begin{Bmatrix} \overline{u_{i-1}} \\ \overline{u_i} \\ \overline{u_{i+1}} \\ \overline{u_{i+2}} \end{Bmatrix} \rightarrow \begin{Bmatrix} b_{20} \\ b_{21} \\ b_{22} \\ b_{23} \end{Bmatrix} = \begin{bmatrix} -1/24 & 13/12 & -1/24 & 0 \\ -7/24 & -5/8 & 9/8 & -5/24 \\ 1/2 & -1 & 1/2 & 0 \\ -1/6 & 1/2 & -1/2 & 1/6 \end{bmatrix} \begin{Bmatrix} \overline{u_{i-1}} \\ \overline{u_i} \\ \overline{u_{i+1}} \\ \overline{u_{i+2}} \end{Bmatrix}$$

$$IS_2 = \left(b_{21} + \frac{1}{4} b_{23} \right)^2 + \frac{13}{3} b_{22}^2 + \frac{781}{20} b_{23}^2$$

$$= \left(\begin{bmatrix} -1/3 \\ -1/2 \\ 1 \\ -1/6 \end{bmatrix}^T \cdot \begin{Bmatrix} \overline{u_{i-1}} \\ \overline{u_i} \\ \overline{u_{i+1}} \\ \overline{u_{i+2}} \end{Bmatrix} \right)^2 + \frac{13}{3} \left(\begin{bmatrix} 1/2 \\ -1 \\ 1/2 \\ 0 \end{bmatrix}^T \cdot \begin{Bmatrix} \overline{u_{i-1}} \\ \overline{u_i} \\ \overline{u_{i+1}} \\ \overline{u_{i+2}} \end{Bmatrix} \right)^2 + \frac{781}{20} \left(\begin{bmatrix} -1/6 \\ 1/2 \\ -1/2 \\ 1/6 \end{bmatrix}^T \cdot \begin{Bmatrix} \overline{u_{i-1}} \\ \overline{u_i} \\ \overline{u_{i+1}} \\ \overline{u_{i+2}} \end{Bmatrix} \right)^2$$

i=3

$$\begin{bmatrix} 1 & 0 & 1/12 & 0 \\ 1 & 1 & 13/12 & 5/4 \\ 1 & 2 & 49/12 & 17/2 \\ 1 & 3 & 109/12 & 111/4 \end{bmatrix} \begin{Bmatrix} b_{30} \\ b_{31} \\ b_{32} \\ b_{33} \end{Bmatrix} = \begin{Bmatrix} \overline{u_i} \\ \overline{u_{i+1}} \\ \overline{u_{i+2}} \\ \overline{u_{i+3}} \end{Bmatrix} \rightarrow \begin{Bmatrix} b_{30} \\ b_{31} \\ b_{32} \\ b_{33} \end{Bmatrix} = \begin{bmatrix} 11/12 & 5/24 & -1/6 & 1/24 \\ -43/24 & 23/8 & -11/8 & 7/24 \\ 1 & -5/2 & 2 & -1/2 \\ -1/6 & 1/2 & -1/2 & 1/6 \end{bmatrix} \begin{Bmatrix} \overline{u_i} \\ \overline{u_{i+1}} \\ \overline{u_{i+2}} \\ \overline{u_{i+3}} \end{Bmatrix}$$

$$IS_3 = \left(b_{31} + \frac{1}{4} b_{33} \right)^2 + \frac{13}{3} b_{32}^2 + \frac{781}{20} b_{33}^2$$

$$= \left(\begin{bmatrix} -11/6 \\ 3 \\ -3/2 \\ 1/3 \end{bmatrix}^T \cdot \begin{Bmatrix} \overline{u_i} \\ \overline{u_{i+1}} \\ \overline{u_{i+2}} \\ \overline{u_{i+3}} \end{Bmatrix} \right)^2 + \frac{13}{3} \left(\begin{bmatrix} 1 \\ -5/2 \\ 2 \\ -1/2 \end{bmatrix}^T \cdot \begin{Bmatrix} \overline{u_i} \\ \overline{u_{i+1}} \\ \overline{u_{i+2}} \\ \overline{u_{i+3}} \end{Bmatrix} \right)^2 + \frac{781}{20} \left(\begin{bmatrix} -1/6 \\ 1/2 \\ -1/2 \\ 1/6 \end{bmatrix}^T \cdot \begin{Bmatrix} \overline{u_i} \\ \overline{u_{i+1}} \\ \overline{u_{i+2}} \\ \overline{u_{i+3}} \end{Bmatrix} \right)^2$$

7 Appendix B

The objective of this section is to show that for $k \geq m-1$ the rational mapping function $g_{\mathrm{RM}}(\omega; k, m, s)$ remains monotonous in the range $\omega, d \in [0,1]$ *regardless* of the value of s. It is important for the monotonicity condition to hold independent of the value of s because s may be varied by the adaptive mapping procedure.

The first derivative of $g_{\mathrm{RM}}(\omega; k, m, s)$ can be expressed in the form a rational function as shown below. The denominator is always positive and, since k is an even integer, $(\omega - d)^k$ is a positive quantity which can be factored out of the numerator. Therefore, it is sufficient to be concerned with the positivity of the term within the curly brackets in the numerator denoted by $n(\omega)$.

$$g'_{\mathrm{RM}}(\omega) = \frac{(\omega-d)^k \overbrace{\left\{(\omega-d)^k + s\left[\omega(1-\omega)\right]^{m-1}\left[(k+1)\omega(1-\omega) - m(\omega-d)(1-2\omega)\right]\right\}}^{n(\omega)}}{\left\{(\omega-d)^k + s\left[\omega(1-\omega)\right]^m\right\}^2}$$

$$n(\omega) = (\omega-d)^k + s\left[\omega(1-\omega)\right]^{m-1} \underbrace{\left\{(2m-1-k)\omega^2 + \left[k+1-m(1+2d)\right]\omega + md\right\}}_{h(\omega)}$$

The first term $(\omega-d)^k$ in $n(\omega)$ is positive. Since $\omega \in [0,1]$, $\omega(1-\omega) \geq 0$. Therefore, $s\left[\omega(1-\omega)\right]^{q-1} \geq 0$ as s is a positive scaling factor. The remaining portion of the second term is a quadratic polynomial in ω denoted by $h(\omega)$.

$h(\omega)$ passes through the points $h(0) = md \geq 0$ and $h(1) = m(1-d) \geq 0$. Hence, if no turning point occurs within the interval $\omega \in [0,1]$, $h(\omega) \geq \min\left[md, m(1-d)\right] \geq 0$. However, if a turning point occurs within the interval, there are two cases to be considered: $k > 2m-1$ and $k < 2m-1$. Note that the case $k = 2m-1$ is invalid since k is an even integer.

Case 1: $k > 2m-1$

Since the coefficient of ω^2 is negative, $h(\omega)$ is a quadratic polynomial with a maximum. Therefore, $h(\omega) \geq \min\left[h(0), h(1)\right] \geq 0$ in the interval $\omega \in [0,1]$.

Case 2: $k < 2m-1$

Since the coefficient of ω^2 is positive, $h(\omega)$ is a quadratic polynomial with a minimum. Let the minimum point of $h(\omega)$ occur at $\omega = \omega_{\min}$.

$$\omega_{\min} = \frac{m(1+2d)-k-1}{2(2m-k-1)}$$

If $\omega_{\min}$ lies beyond the interval $[0,1]$, then $h(\omega)$ is a monotonic positive function within the interval.

Case 2(a): $\omega_{\min} \leq 0 \Rightarrow k \geq m(1+2d)-1$

Case 2(b): $\omega_{\min} \geq 1 \Rightarrow k \geq m(3-2d)-1$

Since $d \in [0,1]$, both cases 2(a) and 2(b) lead to the condition that $k \geq m-1$. Thus, for $k \in [m-1, 2m-1)$, $h(\omega) \geq \min\left[qd, q(1-d)\right] \geq 0$.

This concludes the proof that for $k \geq m-1$, $h(\omega) \geq 0$ which implies that $n(\omega) \geq 0$ and, therefore, $g'_{\mathrm{RM}}(\omega) \geq 0$.

8 Acknowledgements

The authors gratefully acknowledge the support for the present work by Singapore Ministry of Education AcRF Tier-2 grant (MOE2014-T2-1-002), National Supercomputing Center Singapore and support for the first author through Graduate Research Officer scholarship from the School of Mechanical and Aerospace Engineering, Nanyang Technological University, Singapore.

9 References

[1] P.D. Lax, *Hyperbolic systems of conservation laws and the mathematical theory of shock waves*. Vol. 11. 1973: SIAM.

[2] A. Harten. High resolution schemes for hyperbolic conservation laws. *J. Comput. Phys.*, 49:357-393, 1983

[3] A. Harten, B. Engquist, S. Osher, and S.R. Chakravarthy. Uniformly high order accurate essentially non-oscillatory schemes, III. *J. Comput. Phys.*, 71:231-303, 1987

[4] X.-D. Liu, S. Osher, and T. Chan. Weighted Essentially Non-oscillatory Schemes. *J. Comput. Phys.*, 115:200-212, 1994

[5] G.S. Jiang and C.W. Shu. Efficient Implementation of Weighted ENO Schemes. *J. Comput. Phys.*, 126:202-228, 1996

[6] D.S. Balsara and C.W. Shu. Monotonicity Preserving Weighted Essentially Non-oscillatory Schemes with Increasingly High Order of Accuracy. *J. Comput. Phys.*, 160:405-452, 2000

[7] A.K. Henrick, T.D. Aslam, and J.M. Powers. Mapped weighted essentially non-oscillatory schemes: Achieving optimal order near critical points. *J. Comput. Phys.*, 207:542-567, 2005

[8] H. Feng, F. Hu, and R. Wang. A New Mapped Weighted Essentially Non-oscillatory Scheme. *J. Sci. Comput.*, 51:449-473, 2012

[9] H. Feng, C. Huang, and R. Wang. An improved mapped weighted essentially non-oscillatory scheme. *Appl. Math. Comput.*, 232:453-468, 2014

[10] R. Wang, H. Feng, and C. Huang. A New Mapped Weighted Essentially Non-oscillatory Method Using Rational Mapping Function. *J. Sci. Comput.*, 67:540-580, 2016

[11] U S Vevek, B. Zang, and T.H. New. A New Mapped WENO Method for Hyperbolic Problems. in *ICCFD10*. 2018. Barcelona, Spain.

[12] R. Borges, M. Carmona, B. Costa, and W.S. Don. An improved weighted essentially non-oscillatory scheme for hyperbolic conservation laws. *J. Comput. Phys.*, 227:3191-3211, 2008

[13] S. Gottlieb and C.W. Shu. Total variation diminishing Runge-Kutta schemes. *Math. Comp.*, 67:73-85, 1998

[14] D.J. Hill and D.I. Pullin. Hybrid tuned center-difference-WENO method for large eddy simulations in the presence of strong shocks. *J. Comput. Phys.*, 194:435-450, 2004

[15] P.N. Blossey and D.R. Durran. Selective monotonicity preservation in scalar advection. *J. Comput. Phys.*, 227:5160-5183, 2008

[16] J. Qiu and C.W. Shu. On the Construction, Comparison, and Local Characteristic Decomposition for High-Order Central WENO Schemes. *J. Comput. Phys.*, 183:187-209, 2002

[17] C.W. Shu, T.A. Zang, G. Erlebacher, D. Whitaker, and S. Osher. High-order ENO schemes applied to two- and three-dimensional compressible flow. *Applied Numerical Mathematics*. 9:45-71, 1992

[18] E.F. Toro, M. Spruce, and W. Speares. Restoration of the contact surface in the HLL-Riemann solver. *Shock Waves*. 4:25-34, 1994

[19] G.A. Sod. A survey of several finite difference methods for systems of nonlinear hyperbolic conservation laws. *J. Comput. Phys.*, 27:1-31, 1978

[20] C.-W. Shu and S. Osher, Efficient implementation of essentially non-oscillatory shock-capturing schemes, II, *Upwind and High-Resolution Schemes*. 1989, Springer. p. 328-374.

[21] V.A. Titarev and E.F. Toro. Finite-volume WENO schemes for three-dimensional conservation laws. *J. Comput. Phys.*, 201:238-260, 2004

[22] P. Woodward and P. Colella. The numerical simulation of two-dimensional fluid flow with strong shocks. *J. Comput. Phys.*, 54:115-173, 1984

[23] U S Vevek, B. Zang, and T.H. New. On Alternative Setups of the Double Mach Reflection Problem. *J. Sci. Comput.*, 2018